American Journal of
Biomedical Science & Research

www.biomedgrid.com
ISSN: 2642-1747

Research Article

Estimating Three Key Parameters from Measurements in Experiments of Heat Induced Flight

Hongyun Wang[1], Shannon E Foley[2], Hong Zhou[3*]

[1]Department of Applied Mathematics, University of California, USA
[2]Department of Defense, Joint Intermediate Force Capabilities Office, USA
[3]Department of Applied Mathematics, Naval Postgraduate School, USA

*Corresponding Author: Hong Zhou, Department of Applied Mathematics, Naval Postgraduate School, Monterey, CA 93943, USA.

To Cite This Article: *Hongyun Wang, Shannon E Foley and Hong Zhou*. Estimating Three Key Parameters from Measurements in Experiments of Heat Induced Flight. Am J Biomed Sci & Res. 2023 19(2) AJBSR.MS.ID.002563,*
DOI: 10.34297/AJBSR.2023.19.002563

Received: June 08, 2023, **Published:** June 15, 2023

Abstract

We study the problem of heat-induced flight action when a subject is exposed to a millimeter wave beam. There are three key parameters in the model: the nociceptor activation temperature, the subjective threshold for flight initiation, and the human reaction time. We explore mathematical formulations for inferring the three parameters from data measured in exposure tests using the method of limit. We find that the simultaneous inference of the three parameters depends on the experimental design in the sequence of exposure tests. When the beam power density and beam radius of exposure tests span a rectangular region along its two diagonal directions, the three parameters are robustly estimated. Future experiments should consider this pattern of beam power density and beam radius when designing exposure tests. In the case of fluctuating subjective threshold, the medians of three parameters are still reliably estimated when the relative uncertainty in subjective threshold is small or moderate.

Keywords: Heat-induced flight, Activation temperature of thermal nociceptors, Subjective threshold for initiating flight, Human reaction time, Method of limits

Introduction

In cognitive neuroscience one of the main focuses is to understand the underlying mechanism that causes changes in behavior and neural responses through experimental investigation. There are two commonly adopted methods that can help us start psychophysical experiments: the method of limits [1-3] and the method of constant stimuli [1,3,4]. These two methods can be applied to study the response of a human subject exposed to a millimeter wave heating. During millimeter wave exposure, the electromagnetic energy is absorbed by the skin and thereby increases the skin temperature. Once the local temperature of the skin reaches the activation temperature, thermal nociceptors in the skin are activated to transduce an electrical signal. The strength of the total electrical signal is proportional to the number of activated nociceptors. When the pain signal transmitted from nociceptors to the brain is strong enough, the brain issues an instruction signal, directing the muscles to execute a flight action. A flight action here refers to escaping from the electromagnetic beam and/or switching off the beam power. When a test subject is exposed to a time invariant millimeter wave beam, the total amount of activated nociceptors and the electrical signal transduced by the activated nociceptors both rise with the exposure duration. There is a subjective threshold on the exposure duration for the pain signal to reach the subjective tolerance for inducing the flight action. Due to the bio-variability (both the lateral and longitudinal), this subjec-

tive threshold is a random variable, fluctuating from one subject to another and fluctuating from one test to another on the same subject. We view the flight action as initiated when the electrical signal transduced at the exposed skin spot by thermal nociceptors is sufficient for triggering the flight instruction upon propagating to the brain. It takes time for the pain signal to travel from the exposed skin spot to the brain, for the brain to process the pain signal and to issue a flight instruction, and for the muscles to receive the flight instruction and carry out the flight action. As a result, the time of observed flight action is delayed from the time-of-flight initiation. This time delay is the human reaction time.

In our recent work [5] we extracted the median subjective threshold on exposure duration and the human reaction time from data measured in exposure tests designed using the Method of Constant Stimuli (MoCS) where the exposure duration is prescribed in each test. The data collected in a sequence of tests include prescribed exposure durations, observed binary outcomes regarding the occurrence of flight action, and times of observed flight action (if flight occurs). In each test of MoCS, flight action may or may not occur depending on whether the prescribed exposure duration is above or below the sample subjective threshold in that test. In a sequence of exposure tests, the prescription of exposure duration for the next test is updated adaptively based on the prescriptions and outcomes in the tests already completed, using a Bayesian framework. The goal is to probe the system near the median subjective threshold where the human response is most uncertain (about 50% each way). We modeled the random subjective threshold as a Weibull distribution and carried out the inference in two steps. In step 1, we infer the median subjective threshold from the observed binary outcomes, which are independent of the human reaction time. In step 2, we combine the result from step 1 and the times of observed flight action in an inference framework to estimate the deterministic human reaction time. The inference method developed is robust with respect to the discrepancy between the inference model assumed and the actual model of the data. Although the inference method is formulated assuming the Weibull distribution, it yields correct results on the data generated using other distributions for the random subjective threshold. In this paper, we work with data measured in exposure tests designed using the Method of Limits (MoL) where the beam power is kept on and steady until the flight action is observed in each test. The data set contains a sequence of data elements, each corresponding to an individual test. Each data element consists of beam specifications used (beam radius and beam power density), the time series of measured skin surface temperatures (recorded by an IR camera), and the time of observed flight action in an individual test. Previously, we developed a method for reconstructing the skin internal temperature distribution from a time series of surface temperatures [6]. The reconstruction of internal temperature distribution is parameter free. Thus, although the internal temperature distribution is not directly measured in exposure tests, we can regard it as part of the data for inference.

The data of reconstructed skin internal temperatures allow us to examine the process of nociceptor activation and the flight initiation. In this process, there are three key parameters: the activation temperature of thermal nociceptors, the subjective threshold on activated volume for initiating flight and the human reaction time. In this study, we explore the inference of these three key parameters from data in tests of MoL. In each test of MoL, upon the start of beam power, the skin temperature increases monotonically. Thermal nociceptors are activated when the local temperature reaches the activation temperature (which we regard as unknown). Under the assumption that nociceptors are uniformly distributed in skin, the total electrical signal transduced by the nociceptors is proportional to the activated volume where the temperature is above the activation temperature. We use the activated volume to measure the pain signal. There is a subjective threshold on the activated volume.

When this threshold is exceeded, the total electrical signal transduced is sufficient for inducing flight action. We regard this time instance as the flight initiation time. The time of observed flight action is delayed from the flight initiation time by the human reaction time. In a test of MoL, flight action always occurs. The time of observed flight action is influenced by 0) the skin internal temperature distribution, i) the nociceptor activation temperature, ii) the subjective threshold on activated volume for initiating flight, iii) the human reaction time. Item 0) is part of the data we work with; items i)-iii) are the target of our inference analysis. In this study, we focus on the case where both the nociceptor activation temperature and the human reaction are deterministic while the subject threshold on activated volume is allowed to be a random variable, for which we aim at estimating the median. The objective of this study is to develop a mathematical framework for extracting the three key parameters i)-iii) listed above, from data of beam specifications, skin internal temperature distributions, and times of observed flight action measured in tests of MoL. The mathematical framework includes both the inference component and the experimental design component for optimizing the inference. We explore the advantage of having a set of exposure tests spanning a significant range both in the beam radius and in the beam power density used in tests.

Model Of Flight Action in The Method of Limits

Coordinate System and Temperature Distribution

We establish the coordinate system as follows. The skin surface exposed to the millimeter wave is selected as the xy plane with the 2D coordinates denoted by vector $\mathbf{r} = (x, y)$; the depth into the skin is selected as the z-direction. A point in the skin tissue is completely described by its 3D coordinates $(\mathbf{r}, z)$.

Let $T(\mathbf{r}, z, t)$ be the skin temperature at position $(\mathbf{r}, z)$ at time t, which increases monotonically with t upon the start of beam power. We use the notation $\{T(\mathbf{r}, z, t)\}$ to represent the skin internal temperature distribution. In exposure experiments, the skin surface temperature distribution, $\{T(\mathbf{r}, z = 0, t)\}$, is recorded with an IR camera at a sequence of discrete time instances. In a previous study [6], we developed a method for reconstructing the skin internal temperature distribution from a time series of measured skin surface temperatures. The reconstruction method is based solely on the measured surface temperatures; it does not require any parameter values of skin material properties. The reconstruction of skin internal temperature distribution is carried out individually for each exposure test. For this reason, we treat the skin internal temperature distribution as measurable even though it is not directly measured in exposure tests.

Flight Initiation and Flight Actuation as Determined by the Skin Temperature Distribution

Upon the start of beam power, the absorbed electromagnetic energy increases the skin temperature, activates the thermal nociceptors, and produces a heat sensation on the exposed subject. Eventually, when the heat sensation exceeds a threshold, the exposed subject escapes from the beam (we shall call this the flight action) [7,8]. Let $T_{\rm act}$ be the activation temperature of thermal nociceptors. We adopt the model used in [9] that the initiation of flight is governed by the number of activated nociceptors relative to a subjective threshold. Under the assumption that the thermal nociceptors are uniformly distributed in skin tissue, the number of activated nociceptors at time t is directly proportional to the activated volume $V_{\rm act}(t)$, the volume of the 3D region in which the skin temperature at time t is above the activation temperature.

$$\begin{aligned} &V_{\rm act}\Big(t, T_{\rm act}, \{T\}\Big) \\ &\quad \equiv \text{Volume}\left\{ (\mathbf{r}, z) \,\middle|\, T(\mathbf{r}, z, t) \geq T_{\rm act} \right\} \end{aligned} \tag{1}$$

Given the temperature distribution $\big\{T(\mathbf{r}, z, t)\big\}$, the activated volume $\{V_{\rm act}(t)\}$ is determined by the activation temperature $T_{\rm act}$. In exposure tests using the method of limits, the beam power is kept on and steady. The skin temperature and the activated volume increase monotonically with t until the beam power is turned off at the time of flight actuation.

The time of flight initiation is governed by $\{V_{\rm act}(t)\}$ relative to a subjective threshold $v_{\rm c}$ on $V_{\rm act}$. Let $t_{\rm c}$ be the time at which the activated volume reaches the subjective threshold $v_{\rm c}$.

At time $t_{\rm c}$, the electrical signal transduced by thermal nociceptors at the exposed skin spot is strong enough such that after propagating to the brain, it triggers the brain to issue a flight instruction signal to muscles, which eventually actuates the flight action. The process of flight actuation beyond time $t_{\rm c}$ is irreversible. Even if the beam power is turned off right at $t_{\rm c}$, the electrical signal already generated by time $t_{\rm c}$ will still lead to flight action. Thus, we view $t_{\rm c}$ as the time of flight initiation. Mathematically, the flight initiation time $t_{\rm c}$ is governed by

$$V_{\rm act}\Big(t_{\rm c}, T_{\rm act}, \{T\}\Big) = v_{\rm c} \quad \longrightarrow \quad t_{\rm c}\big(T_{\rm act}, v_{\rm c}, \{T\}\big) \tag{2}$$

Given the temperature distribution $\big\{T(\mathbf{r}, z, t)\big\}$, the flight initiation time $t_{\rm c}$ is determined by the activation temperature $T_{\rm act}$ and the subjective volume threshold $v_{\rm c}$.

The flight action occurs at time $t_{\rm F}$, later than the flight initiation time $t_{\rm c}$. The time delay, $t_{\rm R} \equiv t_{\rm F} - t_{\rm c}$, is the human reaction time. We summarize the quantities and functions introduced above.

- $\mathbf{r} = (x, y)$: lateral coordinates on the skin surface.
- z: depth into the skin tissue; $(\mathbf{r}, z)$ is the 3D coordinates of a point in the skin.
- t: time ($t = 0$ is set as the time when the beam power is turned on).
- $T(\mathbf{r}, z, t)$: skin temperature at position $(\mathbf{r}, z)$ at time t.
- $\{T\} \equiv \big\{T(\mathbf{r}, z, t)\big\}$: skin internal temperature distribution.
- $T_{\rm act}$: activation temperature of thermal nociceptors.
- $V_{\rm act}(t) \equiv V_{\rm act}\big(t, T_{\rm act}, \{T\}\big)$: activated volume of skin tissue at time t.
- $v_{\rm c}$: subjective threshold on activated volume for initiating flight.
- $t_{\rm c}$: flight initiation time governed by $V_{\rm act}\big(t, T_{\rm act}, \{T\}\big) = v_{\rm c}$; given temperature distribution $\{T\}$, $t_{\rm c}$ is influenced by parameters $T_{\rm act}$ and $v_{\rm c}$.
- $t_{\rm R}$: human reaction time.
- $t_{\rm F} = t_{\rm c} + t_{\rm R}$: time of observed flight action; given temperature distribution $\{T\}$, $t_{\rm F}$ is influenced by $T_{\rm act}$, $v_{\rm c}$ and $t_{\rm R}$, the three model parameters we want to infer.

Data from exposure tests and inference objectives

In each exposure test, the time of observed flight action $t_{\rm F}$ is recorded while the skin internal temperature distribution $\big\{T(\mathbf{r}, z, t)\big\}$ is indirectly measured, i.e., constructed from a time series of skin surface temperature distributions recorded with an IR camera.

None of $T_{\rm act}$, $v_{\rm c}$, $t_{\rm R}$, $V_{\rm act}(t)$ or $t_{\rm c}$ is directly measurable. We explore the possibility of inferring from measured data the three key parameters: $T_{\rm act}$, $v_{\rm c}$ and $t_{\rm R}$. In this study, we allow $v_{\rm c}$, the subjective volume threshold, to be a random variable, fluctuating from one subject to another and fluctuating from one test to another on the same subject; we assume $T_{\rm act}$ and $t_{\rm R}$ are deterministic unknowns. Our goal is to infer $T_{\rm act}$, median($v_{\rm c}$) and $t_{\rm R}$ from data (Figure 1).

In exposure tests using the method of limits, the data set measured in a sequence of N tests, after post processing, has the form

$$\begin{aligned} \mathrm{D} = \Big\{ \Big(&(t_{\rm F})_j, \{T(\mathbf{r}, z, t)\}_j, (P_d^{(i)})_j, (A_{\rm HM})_j \Big), \\ &j = 1, 2, \ldots, N \Big\} \end{aligned} \tag{3}$$

where $(P_d^{(i)})_j$ is the beam center power density of the incident beam used in test j, and $(A_{\rm HM})_j$ is the half-maximum area of the beam cross-section. Figure 1 illustrates the process from the start of beam power to the observed flight action in an exposure test, based on the model described above. In the process, none of $(T_{\rm act}, V_{\rm act}(t),\ v_{\rm c},\ t_{\rm c},\ t_{\rm R})$ is measurable in real experiments. Only $t_{\rm F}$ and $\{T(\mathbf{r}, z, t)\}$ are measurable and included in data format (3). As we will see, the values of $((P_d^{(i)})_j, (A_{\rm HM})_j)$ are not directly used in the inference of $(T_{\rm act}, v_{\rm c}, t_{\rm R})$. However, a robust inference depends on data from a diversified sequence of exposure tests that spans a significant range in the 2D domain of $\big(\{(P_d^{(i)})_j\}, \{(A_{\rm HM})_j\}\big)$. In particular, if all exposure tests in the sequence use the same beam power density and the same beam spot area, it is impossible to infer more than one parameter.

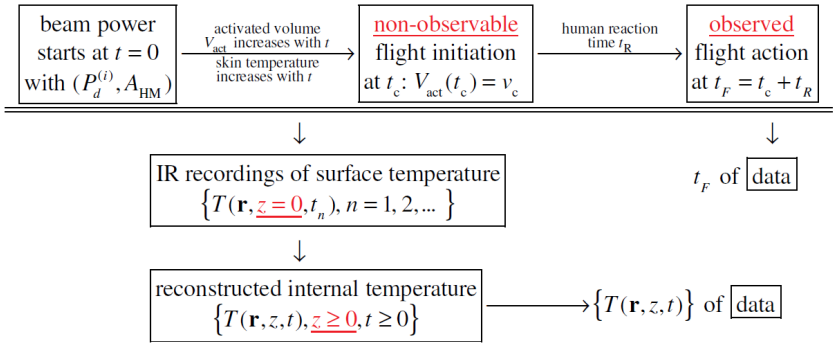

Figure 1: An exposure test using the method of limits. Measurable and non-measurable quantities in the experimental process of inducing flight action.

Model of Experimental Data on Skin Temperature Distribution and Data Generation

Skin Temperature Evolution When Exposed to a Beam

We consider the situation where the skin area of a test subject is exposed to a beam of millimeter wave [10-12]. We adopt a model of skin temperature evolution like that in our previous studies [13-15]. The model is based on the assumptions below.

1. The skin surface exposed to the millimeter wave is flat (the xy plane).
2. The beam ray is along the z-direction, perpendicular to the skin surface.
3. In the xy plane, the beam power density has an axisymmetric Gaussian distribution.

$$P(\mathbf{r}) = P_d^{(i)}\, G(\frac{\mathbf{r}}{r_b}), \quad G(\mathbf{r}) \equiv \exp\left(-2|\mathbf{r}|^2\right) \tag{4}$$

where r_b is the Gaussian beam radius [16]. Here the assumption of axisymmetry is only for simplicity in analysis. The scaling relation between the beam spot area and the activated volume remains the same for all types of beam power distributions.

4. The skin's material properties are uniform in $(z, \mathbf{r})$.
5. The length scale in the lateral directions r_b is much larger than the penetration depth of millimeter wave into the skin (less than 0.5 mm) [17]. In the leading order approximation, the temperature evolution is dominated by the the conduction along the z-direction and the effect of lateral heat conduction is neglected.
6. In exposure tests, the beam power density is selected high enough to ensure that flight action occurs in a short time [7,8]. During this short time period, the cooling effects of blood circulation and heat loss at the skin surface are neglected.
7. Before the start of beam power, the skin's initial temperature is uniform in $(z, \mathbf{r})$, which is called the skin baseline temperature and is denoted by T_{base}.

Let $t = 0$ be the beam start time. The temperature distribution $T(\mathbf{r}, z, t)$ is governed by

$$\begin{cases} \rho_m C_p \dfrac{\partial T}{\partial t} = k\dfrac{\partial^2 T}{\partial z^2} + \alpha P(\mathbf{r})\mu \exp(-\mu z) \\ \left.\dfrac{\partial T}{\partial z}\right|_{z=0} = 0\,, \qquad \left. T\right|_{t=0} = T_{base} \end{cases} \tag{5}$$

Where,

- ρ_m is the mass density of the skin,
- C_p is the specific heat capacity of the skin,
- k is the heat conductivity of the skin,
- μ is the absorption coefficient of the skin for the beam frequency used,
- $P(\mathbf{r})$ is the Gaussian distribution of beam power density in (4), and
- α is the fraction of incident beam power absorbed into the skin.

Since the lateral heat conduction is neglected, (5) does not involve any derivative with respect to lateral coordinate $\mathbf{r}$. The dependence on $\mathbf{r}$ is only in the heat source term via $P(\mathbf{r}) \equiv P_d^{(i)} G(\mathbf{r}/r_b)$. This allows us to write the solution of (5) as

$$T(\mathbf{r}, z, t) = T_{base} + (\alpha P_d^{(i)}) G(\mathbf{r}/r_b) u(z, t) \tag{6}$$

where $u(z, t)$ is the temperature increase per unit of absorbed beam power density and is governed by

$$\begin{cases} \rho_m C_p \dfrac{\partial u}{\partial t} = k\dfrac{\partial^2 u}{\partial z^2} + \mu \exp(-\mu z) \\ \left.\dfrac{\partial u}{\partial z}\right|_{z=0} = 0\,, \qquad \left. u\right|_{t=0} = 0 \end{cases} \tag{7}$$

The activated volume at time t is

$$\begin{aligned} V_{act}(t) &= \text{Volume}\left\{ (\mathbf{r}, z) \middle| T(\mathbf{r}, z, t) \geq T_{act} \right\} \\ &= \text{Volume}\left\{ (\mathbf{r}, z) \middle| (\alpha P_d^{(i)}) G(\mathbf{r}/r_b) u(z, t) \geq (T_{act} - T_{base}) \right\} \end{aligned} \tag{8}$$

Nondimensionalization

The activated volume given in (8) is affected by many parameters:

- the absorbed beam power density ($\alpha P_d^{(i)}$),
- $r_{\rm b}$ in Gaussian distribution $G(\mathbf{r}/r_{\rm b})$,
- ($\rho_{\rm m}$, C_p, k, μ) in the temperature increase per unit of absorbed beam power density $u(z,t)$,
- ($T_{\rm base} - T_{\rm act}$) on the right hand side of the inequality. The initiation of flight is determined by the activated volume relative to the subjective threshold $v_{\rm c}$. In total, there are 9 physical quantities affecting the initiation of flight, namely.

$$(\alpha P_d^{(i)},\, r_{\rm b}),\quad (\rho_{\rm m},\, C_p,\, k,\, \mu),\quad (T_{\rm base},\, T_{\rm act}),\quad v_{\rm c} \tag{9}$$

To reveal the roles and interactions of these physical quantities in initiating flight action, and to simplify the mathematical formulation, we carry out non-dimensionalization. For each physical quantity, we introduce a scale for its physical dimension and write out the corresponding non-dimensional quantity.

- Temperature scale is the difference between a characteristic activation temperature $T_{\rm act}^{(0)}$ and the baseline temperature $T_{\rm base}$. The true $T_{\rm act}$ may deviate from $T_{\rm act}^{(0)}$.

$$\Delta T_{\rm s} = \left(T_{\rm act}^{(0)} - T_{\rm base}\right),\qquad T_{\rm nd} = \frac{T - T_{\rm base}}{\Delta T_{\rm s}}$$

$$T_{\rm act,nd}^{(0)} = \frac{T_{\rm act}^{(0)} - T_{\rm base}}{\Delta T_{\rm s}} = 1\,,$$
$$T_{\rm act,nd} = \frac{T_{\rm act} - T_{\rm base}}{\Delta T_{\rm s}} \neq 1 \text{ (possibly)}$$

- Length scale in the depth direction is provided by, $1/\mu$, the characteristic penetration depth of millimeter wave into the skin.

$$z_{\rm s} = \frac{1}{\mu}\,,\qquad z_{\rm nd} = \frac{z}{z_{\rm s}}$$

- Length scale in the lateral directions is obtained from a characteristic volume threshold $v_{\rm c}^{(0)}$. The true volume threshold $v_{\rm c}$ may deviate from $v_{\rm c}^{(0)}$.

$$r_{\rm s} = \sqrt{\frac{v_{\rm c}^{(0)}}{\pi z_{\rm s}}} = \sqrt{\frac{\mu v_{\rm c}^{(0)}}{\pi}}\,,\qquad \mathbf{r}_{\rm nd} = \frac{\mathbf{r}}{r_{\rm s}}$$

  Geometrically, $r_{\rm s}$ is the radius of the cylinder with volume $v_{\rm c}^{(0)}$ and height $z_{\rm s}$.

- Volume scale is provided by the combination $r_{\rm s}^2 z_{\rm s}$.

$$v_{\rm s} = r_{\rm s}^2 z_{\rm s} = \frac{v_{\rm c}^{(0)}}{\pi}\,,\qquad V_{\rm nd} = \frac{V}{v_{\rm s}}$$

$$v_{\rm c,nd}^{(0)} = \frac{v_{\rm c}^{(0)}}{v_{\rm s}} = \pi\,,\qquad v_{\rm c,nd} = \frac{v_{\rm c}}{v_{\rm s}} \neq \pi \text{ (possibly)}$$

- Time scale is derived from skin material properties.

$$t_{\rm s} = \frac{\rho_{\rm m} C_p}{k\mu^2}\,,\qquad t_{\rm nd} = \frac{t}{t_{\rm s}}$$

- Power density scale is derived from $v_{\rm s}$, $(\rho_{\rm m} C_p)$, $\Delta T_{\rm s}$, $r_{\rm s}$, and t_s.

$$P_{\rm s} = \frac{v_s(\rho_{\rm m} C_p)\Delta T_{\rm s}}{r_s^2\, t_s} = k\mu \Delta T_{\rm s}\,,\qquad P_{\rm nd} = \frac{P}{P_{\rm s}}$$

- Scale for $u \equiv (T - T_{\rm base})/(\alpha P)$, temperature per power density, is

$$u_{\rm s} = \frac{\Delta T_{\rm s}}{P_{\rm s}} = \frac{1}{k\mu}\,,\qquad u_{\rm nd} = \frac{u}{u_{\rm s}}$$

- Energy scale is built based on $P_{\rm s}$, $t_{\rm s}$, and $r_{\rm s}$.

$$E_{\rm s} = P_{\rm s}\, r_{\rm s}^2\, t_{\rm s} = \frac{v_{\rm c}^{(0)}}{\pi}(\rho_{\rm m} C_p)\Delta T_{\rm s}\,,\qquad E_{\rm nd} = \frac{E}{E_{\rm s}}$$

We need to point out that in the non-dimensionalization above, we used a characteristic activation temperature $T_{\rm act}^{(0)}$ and a characteristic volume threshold $v_{\rm c}^{(0)}$. The actual values of $(T_{\rm act}, v_{\rm c})$ may deviate from $(T_{\rm act}^{(0)}, v_{\rm c}^{(0)})$.

For simplicity, we shall drop the subscript $_{\rm nd}$ in all non-dimensional quantities. Instead, the original physical quantities will be distinguished with subscript $_{\rm phy}$, when necessary for clarity. For example, $P_d^{(i)}$ refers to the non-dimensional beam center power density while $P_{\rm d,phy}^{(i)}$ is the physical beam center power density before non-dimensionalization. With this notation, the non-dimensional versions of baseline temperature, characteristic activation temperature and characteristic volume threshold are

$$T_{\rm base} = 0\,,\qquad T_{\rm act}^{(0)} = 1\,,\qquad v_{\rm c}^{(0)} = \pi \tag{10}$$

The non-dimensional version of true $(T_{\rm act}, v_{\rm c})$ may deviate from $(T_{\rm act}^{(0)}, v_{\rm c}^{(0)})$.

$$T_{\rm act} = \frac{T_{\rm act,phy} - T_{\rm base,phy}}{T_{\rm act,phy}^{(0)} - T_{\rm base,phy}}\,,\qquad v_{\rm c} = \pi\frac{v_{\rm c,phy}}{v_{\rm c,phy}^{(0)}} \tag{11}$$

After nondimensionalization, (7), the evolution equation of the temperature increase per beam power density $u(z,t)$ becomes

$$\begin{cases} \dfrac{\partial u}{\partial t} = \dfrac{\partial^2 u}{\partial z^2} + \exp(-z) \\ \dfrac{\partial u}{\partial z}\Big|_{z=0} = 0\,,\qquad u\Big|_{t=0} = 0 \end{cases} \tag{12}$$

Equation (12) is parameter free. Its solution has a closed-form expression [18].

$$u(z,t) = \begin{cases} -e^{-z} - z\,\mathrm{erfc}\frac{z}{2\sqrt{t}} + \frac{2\sqrt{t}}{\sqrt{\pi}} e^{\frac{-z^2}{4t}} + \frac{e^{t-z}}{2}\mathrm{erfc}\frac{2t-z}{2\sqrt{t}} + \frac{e^{t+z}}{2}\mathrm{erfc}\frac{2t+z}{2\sqrt{t}}, \\ 0, \end{cases} \tag{13}$$

where $\mathrm{erfc}(u)$ is the complementary error function defined as

$$\mathrm{erfc}(u) \equiv \frac{2}{\sqrt{\pi}}\int_u^{+\infty} e^{-s^2} ds \tag{14}$$

The absorption fraction α and the beam center power density $P_d^{(i)}$ appear only in the combination $(\alpha P_d^{(i)})$. For conciseness, we rename the combination as $P_d \equiv (\alpha P_d^{(i)})$. It follows from (6) that the non-dimensional temperature distribution is completely described by parameters (P_d, r_b) and has the expression.

$$T\big(\mathbf{r}, z, t; P_d, r_\mathrm{b}\big) = P_d G(\mathbf{r}/r_\mathrm{b}) u(z,t) \tag{15}$$

where the non-dimensional version of (P_d, r_b) is

$$r_\mathrm{b} = r_{\mathrm{b,phy}} \sqrt{\frac{\pi}{\mu\, v_{\mathrm{c,phy}}^{(0)}}}\,, \qquad \alpha P_d^{(i)} = \frac{\alpha P_{\mathrm{d,phy}}^{(i)}}{k\mu\left(T_{\mathrm{act,phy}}^{(0)} - T_{\mathrm{base,phy}}\right)} \tag{16}$$

The corresponding non-dimensional activated volume at time t is

$$V_\mathrm{act}(t; T_\mathrm{act}, P_d, r_\mathrm{b}) = \mathrm{Volume}\left\{ (\mathbf{r}, z) \,\middle|\, P_d G(\mathbf{r}/r_\mathrm{b}) u(z,t) \geq T_\mathrm{act} \right\} \tag{17}$$

A change of variables $\mathbf{r}_\mathrm{new} = \mathbf{r}_\mathrm{old}/r_\mathrm{b}$ separates out the dependence on r_b.

$$V_\mathrm{act}(t; T_\mathrm{act}, P_d, r_\mathrm{b}) = r_\mathrm{b}^2\, V_\mathrm{act}(t; T_\mathrm{act}/P_d) \tag{18}$$

$$\text{where}\quad V_\mathrm{act}(t; T_\mathrm{act}/P_d) \equiv \mathrm{Volume}\left\{ (\mathbf{r}, z) \,\middle|\, G(\mathbf{r}) u(z,t) \geq T_\mathrm{act}/P_d \right\}$$

Scaling relation (18) greatly simplifies the calculation of $V_\mathrm{act}(t)$ for various values of $(T_\mathrm{act}, P_d, r_\mathrm{b})$.

The temperature per unit power density $u(z,t)$ in (13) increases monotonically with t.

$$\frac{\partial u(z,t)}{\partial t} = \frac{e^{t-z}}{2}\mathrm{erfc}\frac{2t-z}{2\sqrt{t}} + \frac{e^{t+z}}{2}\mathrm{erfc}\frac{2t+z}{2\sqrt{t}} > 0\,, \quad t > 0 \tag{19}$$

It follows that the activated volume $V_\mathrm{act}(t)$ increases monotonically with t. Flight is irreversibly initiated at t_c when $V_\mathrm{act}(t)$ reaches the subjective threshold v_c. The flight initiation time t_c is related to parameters $(T_\mathrm{act}, v_\mathrm{c}, P_d, r_\mathrm{b})$ in the equation below

$$V_\mathrm{act}\Big(t_\mathrm{c}; T_\mathrm{act}, P_d, r_\mathrm{b}\Big) = v_\mathrm{c} \tag{20}$$

Upon being initiated at time t_c, flight is eventually materialized and observed at time $t_\mathrm{F} = t_\mathrm{c} + t_\mathrm{R} > t_\mathrm{c}$ where t_R is the human reaction time.

In summary, from the start of beam power to the time of observed flight action, the non-dimensional process has only 5 parameters: $(T_\mathrm{act}, v_\mathrm{c}, t_\mathrm{R}, P_d, r_\mathrm{b})$, in which (P_d, r_b) are the beam specifications that we select in experimental design; $(T_\mathrm{act}, v_\mathrm{c}, t_\mathrm{R})$ are the unknown parameters we try to infer from data of $\big(t_\mathrm{F}, \{T\}\big)$.

Model of the randomness in subjective threshold v_c

Of the three key model parameters $(T_\mathrm{act}, v_\mathrm{c}, t_\mathrm{R})$, in this study, we assume the activation temperature T_act and the human reaction time t_R are deterministic while allowing the subjective threshold v_c to be a random variable. The objective of our inference is to estimate the deterministic quantities $(T_\mathrm{act}, v_\mathrm{c}^{(\mathrm{m})}, t_\mathrm{R})$ where $v_\mathrm{c}^{(\mathrm{m})} \equiv \mathrm{median}(v_\mathrm{c})$. In our numerical simulations, we test inference performance on data sets generated respectively from a Weibull distribution or from a log-normal distribution for v_c.

- Weibull distribution for v_c

$$v_\mathrm{c} = v_\mathrm{c}^{(\mathrm{m})} Z\,, \qquad Z \sim \mathrm{Weibull}(\lambda, k)\,, \qquad \lambda = \frac{1}{(\ln 2)^{1/k}} \tag{21}$$

  The scale parameter λ is related to the shape parameter k as given above to make $\mathrm{median}(Z) = 1$. Random variable Z has only one parameter k, which governs the distribution width. The relative standard deviation of v_c is

$$\frac{\mathrm{std}(v_\mathrm{c})}{\mathrm{median}(v_\mathrm{c})} = \mathrm{std}(Z) = \frac{\sqrt{\Gamma(1+2/k) - \Gamma(1+1/k)^2}}{(\ln 2)^{1/k}}$$

- Log-normal distribution for v_c

$$v_\mathrm{c} = v_\mathrm{c}^{(\mathrm{m})} Z\,, \qquad Z \sim \text{Log-normal}(0, \sigma^2) \tag{22}$$

  Random variable Z satisfies $\mathrm{median}(Z) = 1$ and has only one parameter σ, which governs the distribution width. The relative standard deviation of v_c is

$$\frac{\mathrm{std}(v_\mathrm{c})}{\mathrm{median}(v_\mathrm{c})} = \mathrm{std}(Z) = e^{\sigma^2/2}\sqrt{e^{\sigma^2} - 1}$$

Generating Artificial Data Based on the Model

The non-dimensionalization in the previous subsection is based on $(T_\mathrm{act}^{(0)}, v_\mathrm{c}^{(0)})$, a characteristic activation temperature and a characteristic volume threshold. This approach simplifies the formulation and at the same time allows us to consider the true activation temperature and the true volume threshold $(T_\mathrm{act}, v_\mathrm{c})$ as unknown parameters in the system. We will generate data and carry out inference analysis in this non-dimensional system. At the end, we will show that the inference methods developed are invariant under scaling. Thus, the inference methods developed are directly applicable to real experimental data.

We generate artificial data sets of the format described in (3). The incident beam power density $P_d^{(i)}$ is directly proportional to the absorbed beam power density P_d. The half maximum area of beam spot A_HM is proportional to r_b^2, the square of beam radius.

$$P_d^{(i)} = \frac{1}{\alpha} P_d\,, \quad A_\mathrm{HM} = \frac{\ln 2}{2}\pi r_\mathrm{b}^2$$

For simplicity we adopt the format in (23) for artificial data sets.

$$\mathrm{D} = \left\{ \Big((t_\mathrm{F})_j, \{T(\mathbf{r}, z, t)\}_j, (P_d)_j, (r_\mathrm{b})_j \Big),\ j = 1, 2, \ldots, N \right\} \tag{23}$$

This change in data format does not affect the inference. We use the values of $\{(P_d)_j, (r_b)_j\}$ only to indicate the diversity of exposure tests in beam power density and in beam spot size.

The values of $\{(P_d)_j, (r_b)_j\}$ do not actually enter into the inference computation.

We use the parameters below in our data generation.

$$T_{act} = 1, \quad v_c^{(m)} = \pi, \quad t_R = 1, \quad \sigma = \text{variable} \tag{24}$$

An artificial data set consists of data elements from a sequence of exposure tests, each data element containing the results of an individual test. These tests are divided into groups accordingly to their values of (P_d, r_b). We follow the steps below to generate the data element for each individual test.

i) For each test, select (P_d, r_b) according to the experimental design.

ii) With (P_d, r_b), build the temperature distribution $\{T(\mathbf{r}, z, t)\}$ in (15), which corresponds to the skin internal temperature distribution reconstructed from the time series of skin surface temperatures measured in a real test.

iii) With $\{T(\mathbf{r}, z, t)\}$ and T_{act}, calculate the activated volume $\{V_{act}(t)\}$ in (18).

iv) Draw a random sample of v_c according to distribution (21,22).

v) With $\{V_{act}(t)\}$ and v_c, solve for the flight initiation time t_c in (20).

vi) With t_c and t_R, calculate the flight actuation time $t_F = t_c + t_R$.

vii) The data element for the test is $\big(t_F, \{T(\mathbf{r}, z, t)\}, P_d, r_b\big)$.

For each test in the data generation, a sample of v_c is drawn from distribution (21,22). The sample is used to calculate t_c, which leads to t_F. While t_F is recorded in data, neither v_c nor t_c is included in data because neither is measurable in experiments. To emulate the situation of real exposure tests, the artificial data include only the measurable quantities.

Mathematical Formulation and Experimental Design for Inference

We explore mathematical formulations for inferring (T_{act}, v_c, t_R) from a given data set. Since not all data sets contain the necessary information for determining (T_{act}, v_c, t_R), we also examine the experimental design behind the data collection/generation to optimize the inference performance. In this section, for simplicity, we work with data sets generated using deterministic v_c (i.e., $v_c = v_c^{(m)}$ in (21) and (22)).

Our general strategy is to analyze the ensemble behavior of the activated volume. In each individual tests, we calculate the activated volume using trial parameter values. Then we study the ensemble behavior of activated volume over all exposure tests. This ensemble behavior is the key in revealing information about our inference target (T_{act}, v_c, t_R), and is highly influenced by the diversity of the exposure tests in (P_d, r_b). Specifically, we focus on the predicted activated volume at the predicted time of flight initiation because this quantity is invariant over all exposure tests when the trial parameter values used in predicting the activated volume coincide with the true parameter values.

Given the skin temperature distribution in data, the activated volume as a function of t is readily calculated when a trial value of the activation temperature T_{act} is supplied (Figure 2). The time of flight initiation is predicted from the time of observed flight action in data and a trial value of the human reaction time t_R (Figure 2). Combining the two steps, we predict the activated volume at flight initiation for each pair of trial values of (T_{act}, t_R).

In each individual exposure test, the predicted activated volume at flight initiation is a function of $(T_{act}^{(trial)}, t_R^{(trial)})$. From a data set containing a sequence of tests, we obtain a collection of such functions, one for each test.

Activated volume at flight initiation V_c calculated from data using trial values of (T_{act}, t_R)

Let V_c denote the activated volume at the time of flight initiation,

$$V_c \equiv V_{act}(t_c) \tag{25}$$

Given the skin temperature distribution in data (23), the calculation of V_c in (25) depends on the activation temperature T_{act} and the time of flight initiation $t_c = t_F - t_R$ where t_F is the time of observed flight action given in data. Thus, given the data of an individual test, the calculation of V_c in (25) is completely specified by the trial values of (T_{act}, t_R). Figure 2 illustrates the 3 steps in calculating V_c from data.

i) Given a trial value of activation temperature $T_{act}^{(trial)}$, the temperature distribution $\{T(\mathbf{r}, z, t)\}$ in data produces $\{V_{act}(t; T_{act}^{(trial)})\}$.

ii) Given a trial value of the human reaction time $t_R^{(trial)}$, the time of observed flight actuation t_F in data gives $t_c = t_F - t_R^{(trial)}$.

iii) Combining $\{V_{act}(t)\}$ and t_c, we obtain $V_c(T_{act}^{(trial)}, t_R^{(trial)}) \equiv V_{act}(t_c; T_{act}^{(trial)})$.

For conciseness, we drop the superscript $^{(trial)}$ and denote the trial values simply by (T_{act}, t_R). Data set (23) contains a sequence of N exposure tests. From the data of test j, we calculate the two-variable function $V_{c,j}(T_{act}, t_R)$, the activated volume at flight initiation predicted using trial values (T_{act}, t_R). The calculated function $V_{c,j}(T_{act}, t_R)$ is specific to test j and is affected by the beam parameters (r_b, P_d) used in test j. For data set (23), we have a family of N calculated $V_{c,j}(T_{act}, t_R)$.

$$\{V_{c,j}(T_{act}, t_R)\ , \quad j = 1, 2, \ldots, N\} \tag{26}$$

Note that the true volume threshold v_c is the true activated volume at the true time of flight initiation, all of which are unknown. The calculation of $V_{c,j}(T_{act}, t_R)$ does not require v_c. The unknown v_c and the family of calculated functions (26) are related by

$$V_{c,j}(T_{act}^{(true)}, t_R^{(true)}) = v_c\ , \quad j = 1, 2, \ldots, N \tag{27}$$

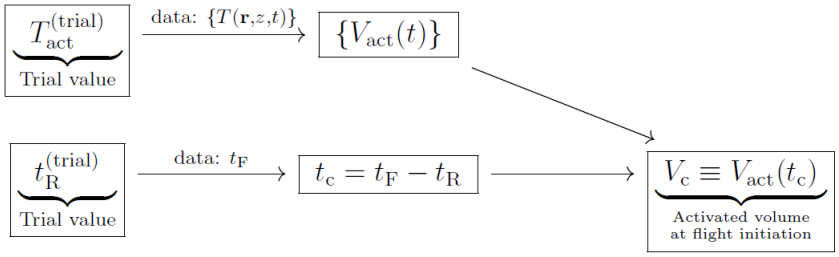

Figure 2: The activated volume at flight initiation, calculated from data $\big(\{T(\mathbf{r},z,t)\}, t_{\rm F}\big)$, as a function of trial parameters $(T_{\rm act}^{\rm (trial)}, t_{\rm R}^{\rm (trial)})$.

At each point in the 2D space of $(T_{\rm act}, t_{\rm R})$, (26) gives a set of N calculated values of $V_{{\rm c},j}$. We study the normalized sample standard deviation of the set, S_V, defined below.

$$\begin{aligned}
&{\rm std}\big\{V_{{\rm c},j}\big\} \equiv {\rm std}\big\{V_{{\rm c},j}(T_{\rm act}, t_{\rm R}),\ j = 1, 2, \ldots, N\big\} \\
&{\rm mean}\big\{V_{{\rm c},j}\big\} \equiv {\rm mean}\big\{V_{{\rm c},j}(T_{\rm act}, t_{\rm R}),\ j = 1, 2, \ldots, N\big\} \\
&d \equiv \max\big(0, \delta - {\rm mean}\big\{V_{{\rm c},j}\big\}\big) \\
&S_V(T_{\rm act}, t_{\rm R}) \equiv \frac{{\rm std}\big\{V_{{\rm c},j}\big\} + d}{{\rm mean}\big\{V_{{\rm c},j}\big\} + d^2}
\end{aligned} \tag{28}$$

where δ is a tiny number much smaller than the true volume threshold $v_{\rm c}$ (e.g., $\delta = 10^{-40}$). At true values $(T_{\rm act}^{\rm (true)}, t_{\rm R}^{\rm (true)})$, (27) gives

$$\begin{aligned}
&{\rm std}\big\{V_{{\rm c},j}\big\} = 0\,, \quad {\rm mean}\big\{V_{{\rm c},j}\big\} = v_{\rm c} > \delta\,, \quad d = 0 \\
&S_V(T_{\rm act}^{\rm (true)}, t_{\rm R}^{\rm (true)}) = \frac{0 + 0}{v_{\rm c} + 0} = 0
\end{aligned} \tag{29}$$

Since $S_V(T_{\rm act}, t_{\rm R}) \geq 0$ everywhere, we estimate $(T_{\rm act}^{\rm (true)}, t_{\rm R}^{\rm (true)})$ by minimizing S_V.

$$(T_{\rm act}^{\rm (est)}, t_{\rm R}^{\rm (est)}) = \underset{(T_{\rm act}, t_{\rm R})}{\rm argmin}\ S_V(T_{\rm act}, t_{\rm R}) \tag{30}$$

Once $(T_{\rm act}^{\rm (est)}, t_{\rm R}^{\rm (est)})$ is obtained, we estimate $v_{\rm c}^{\rm (m)} \equiv {\rm median}(v_{\rm c})$ as

$$v_{\rm c}^{\rm (m,est)} = {\rm median}\big\{V_{{\rm c},j}(T_{\rm act}^{\rm (est)}, t_{\rm R}^{\rm (est)})\big\} \tag{31}$$

(Eq 28), (Eq 30) and (Eq 31) provide the mathematical foundation for inferring $(T_{\rm act}^{\rm (true)}, t_{\rm R}^{\rm (true)}, v_{\rm c}^{\rm (m)})$.

The definition of S_V in (28) is selected for two purposes:

1. we normalize the std to measure the relative changes in $V_{\rm c}$ instead of the absolute changes;
2. we use a tiny number δ to mitigate the singularity when ${\rm mean}\{V_{{\rm c},j}\} = 0$.

This singularity occurs when the trial value of $T_{\rm act}$ is too high. At a high activation temperature, no nociceptor is activated and the predicted activated volume is zero for all tests in the data set. As a result, we have ${\rm mean}\{V_{{\rm c},j}\} = 0$, ${\rm std}\{V_{{\rm c},j}\} = 0$ and $d = \delta$ for large $T_{\rm act}$. To make the minimum in (30) uniquely and robustly defined at the true target $(T_{\rm act}^{\rm (true)}, t_{\rm R}^{\rm (true)})$, we use a tiny number δ to make $S_V(T_{\rm act}, t_{\rm R})$ large for large $T_{\rm act}$.

Calculated $S_V(T_{\rm act}, t_{\rm R})$ on a data set spanning a range of power density at a fixed beam radius

As described in equation (30), our approach of estimating $(T_{\rm act}^{\rm (true)}, t_{\rm R}^{\rm (true)})$ is to minimize the two-variable function $S_V(T_{\rm act}, t_{\rm R})$, which is calculated from data. The success of this approach depends on that $S_V(T_{\rm act}, t_{\rm R})$ has a uniquely defined minimum. In particular, we need $S_V(T_{\rm act}, t_{\rm R}) > 0$ away from $(T_{\rm act}^{\rm (true)}, t_{\rm R}^{\rm (true)})$. This requires that the exposure tests in the data set span a significant range in the beam power density P_d direction and/or in the beam radius r_b direction. In the absence of noise/uncertainty, if all tests in a data set have the same (P_d, r_b), then all tests will produce the same temperature distribution of $\{T\}$ and the same value of $t_{\rm F}$, which yields the same calculated value of $V_{\rm c,j}(T_{\rm act}, t_{\rm R})$ for all j. It leads to ${\rm std}\{V_{\rm c}\} = 0$ everywhere and $S_V(T_{\rm act}, t_{\rm R}) = 0$ in the parameter region where ${\rm mean}\{V_{\rm c}\} > \delta$, which is a large region in $(T_{\rm act}, t_{\rm R})$. To make $S_V = 0$ only at $(T_{\rm act}^{\rm (true)}, t_{\rm R}^{\rm (true)})$, the exposure tests need to have a significant diversity in (P_d, r_b).

In this subsection, we study $S_V(T_{\rm act}, t_{\rm R})$ on a data set spanning a range of P_d at a fixed r_b. Figure 3 shows the $(r_{\rm b}, P_d)$-distribution of the data set (left panel) and the contour plot of $S_V(T_{\rm act}, t_{\rm R})$ calculated from the data set (right panel). From the contour plot, we see that the minimum of $S_V(T_{\rm act}, t_{\rm R})$ in the 2D space of $(T_{\rm act}, t_{\rm R})$ is practically attained everywhere in a slender ellipse, which is approximately aligned with the $T_{\rm act}$ direction. The 2D minimum is not robustly defined. We study the problem of determining one of $(T_{\rm act}, t_{\rm R})$ while the other is known. When $t_{\rm R} = 1$ is given, the plot of S_V vs $T_{\rm act}$ is fairly flat (left panel of Figure 4). In contrast, when $T_{\rm act} = 1$ is given, the plot of S_V vs $t_{\rm R}$ has a well-defined minimum (right panel of Figure 4).

Conclusions of Figures 3 and 4

We examine the inference of $(T_{\rm act}, t_{\rm R})$ from a data set of exposure tests spanning a range of power density at a fixed beam radius. This data set is ineffective for inferring $(T_{\rm act}, t_{\rm R})$ simultaneously. The 2D inference is susceptible to noise and errors. The activation temperature $T_{\rm act}$ is not robustly determined even if the true human reaction time $t_{\rm R} = 1$ is given. On the other hand, if the true activation temperature $T_{\rm act} = 1$ is given, the human reaction time $t_{\rm R}$ is very well-determined.

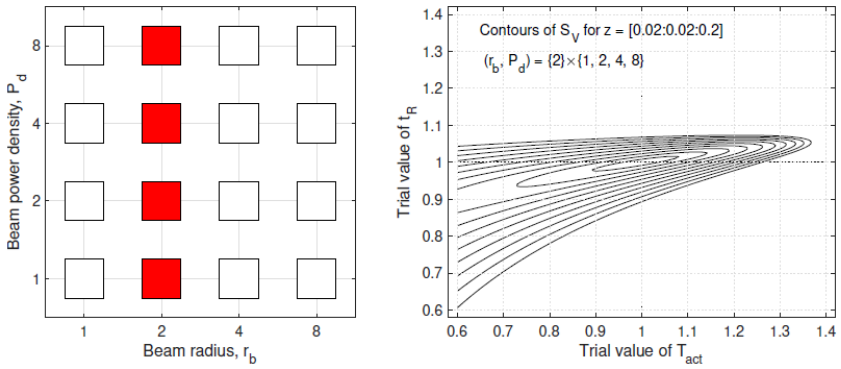

Figure 3: Left: $(r_{\rm b}, P_d)$-distribution of the data set spanning a range of P_d at a fixed $r_{\rm b}$. Right: contours of S_V vs $(T_{\rm act}, t_{\rm R})$ based on the data set.

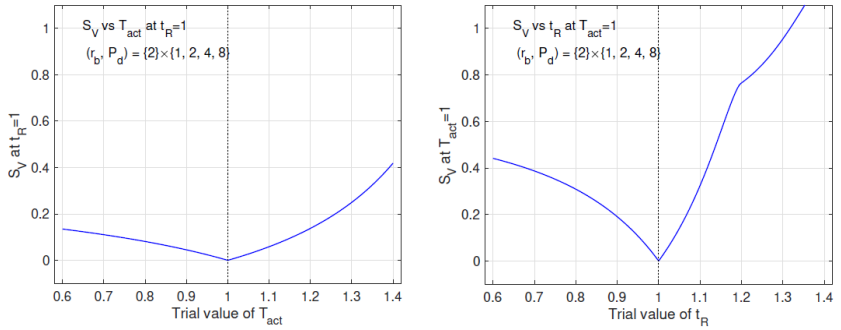

Figure 4: Left: S_V vs $T_{\rm act}$ at $t_{\rm R} = 1$ based on the same data as in Figure 1. Right: S_V vs $t_{\rm R}$ at $T_{\rm act} = 1$.

Calculated $S_V(T_{\rm act}, t_{\rm R})$ on a data set spanning a range of beam radius at a fixed power density

In this subsection, we study $S_V(T_{\rm act}, t_{\rm R})$ on a data set spanning a range of r_b at a fixed P_d. Figure 5 shows the $(r_{\rm b}, P_d)$-distribution of the data set (left panel) and the contour plot of $S_V(T_{\rm act}, t_{\rm R})$ calculated from the data set (right panel). From the contour plot, we see that the minimum of S_V in the 2D space of $(T_{\rm act}, t_{\rm R})$ is not well-defined at all. The minimum is virtually attained everywhere in a straight deep valley along the angular direction of $3\pi/4$. We study the problem of determining one of $(T_{\rm act}, t_{\rm R})$ while the other is known. When $t_{\rm R} = 1$ is given, the plot of S_V vs $T_{\rm act}$ has a well-defined minimum (left panel of Figure 6). Similarly, when $T_{\rm act} = 1$ is given, the plot of S_V vs $t_{\rm R}$ also demonstrates a well-defined minimum (right panel of Figure 6).

Conclusions of Figures 5 and 6. We examine the inference of $(T_{\rm act}, t_{\rm R})$ from a data set of exposure tests spanning a range of beam radius at a fixed power density. This data set does not contain enough information for inferring $(T_{\rm act}, t_{\rm R})$ simultaneously. Only the combination $(T_{\rm act} + t_{\rm R})$ is accurately extracted from the data while $(T_{\rm act} - t_{\rm R})$ is virtually undetermined. However, if one of $(T_{\rm act}, t_{\rm R})$ is given, the other is very well-determined.

Calculated $S_V(T_{\rm act}, t_{\rm R})$ on data sets with more widespread $(r_{\rm b}, P_d)$-distributions

To infer $(T_{\rm act}, t_{\rm R})$ simultaneously, we need data sets of exposure tests with more diversity in $(r_{\rm b}, P_d)$. We examine the inference performance of 3 different data sets, each covering the 2D region of $(r_{\rm b}, P_d)$ in some way. In Figure 7, we consider the data set of 7 pairs of beam parameters covering both the beam radius and the power density directions but not the 4 corners of the 2D region (left panel). Due to its diversity in both $r_{\rm b}$ and P_d, this data set produces a well-defined minimum of S_V in the 2D space of $(T_{\rm act}, t_{\rm R})$ (right panel). In Figure 8, we examine the full data set containing all 16 pairs of beam parameters in the entire 2D region of $(r_{\rm b}, P_d)$ (left panel). Not surprisingly, the minimum of S_V in the 2D space of $(T_{\rm act}, t_{\rm R})$ is much better defined based on this data set (right panel). When $(T_{\rm act}, t_{\rm R})$ moves away from $(T_{\rm act}^{\rm (true)}, t_{\rm R}^{\rm (true)})$, the value of S_V increases much more rapidly in Figure 8 than in Figure 7, which makes the inference more robust with respect to noise and errors. Next we explore achieving the inference robustness of Figure 8 with fewer than 16 pairs of beam parameters. In Figure 9, the experimental design uses 8 pairs of beam parameters to cover the two diagonals of the 2D region, which include the 4 corners (left panel). Because of this excellent diversity in $(r_{\rm b}, P_d)$, the data set in Figure 9 leads to both an excellent robustness and a good efficiency in inferring $(T_{\rm act}, t_{\rm R})$ (right panel).

Conclusions of Figures 7,8 and 9
We examine the simultaneous inference of $(T_{\rm act}, t_{\rm R})$ from a data set of exposure tests covering the 2D region of beam radius and power density. The 2D inference is well-defined and robust as long as the data set covers the 2D region in a genuine way. The most effective data set for inference consists of exposure tests with the $(r_{\rm b}, P_d)$-distribution covering the two diagonals of the 2D region, as illustrated in the left panel of Figure 9. We shall use this $(r_{\rm b}, P_d)$-distribution in our numerical tests with noise.

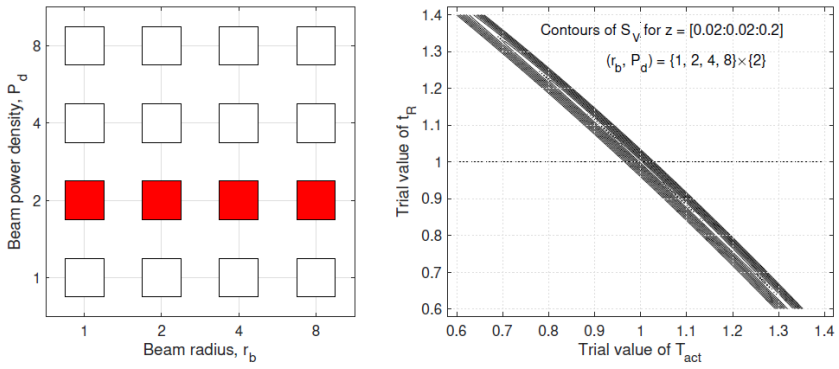

Figure 5: Left: $(r_{\rm b}, P_d)$-distribution of the data set spanning a range of $r_{\rm b}$ at a fixed P_d. Right: contours of S_V vs $(T_{\rm act}, t_{\rm R})$ based on the data set.

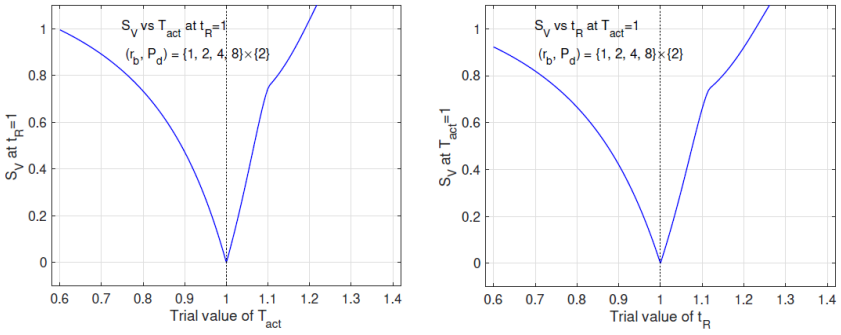

Figure 6: Left: S_V vs $T_{\rm act}$ at $t_{\rm R} = 1$ based on the same data as in Figure 3. Right: S_V vs $t_{\rm R}$ at $T_{\rm act} = 1$.

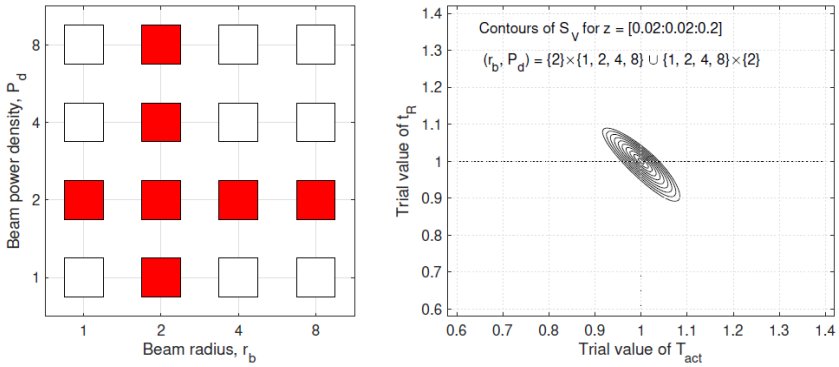

Figure 7: Left: $(r_{\rm b}, P_d)$-distribution of the data set from 7 pairs of beam parameters covering the horizontal and vertical directions of the 2D region. Right: contours of S_V vs $(T_{\rm act}, t_{\rm R})$ based on the data set.

Inference performance on data with fluctuating $v_{\rm c}$

In this section, we test the performance of the inference method developed in Section 4 on data generated with fluctuating $v_{\rm c}$, the subjective threshold on activated volume. The randomness of $v_{\rm c}$ is modeled as distribution (21) or (22).

Summary of the Inference Method and Experimental Design

Our inference approach formulated in Section 4 consists of the steps below.

i) In a data set of form (23), for test j, we calculate the activated volume at flight initiation $V_{\rm c,j}$, using trial values of $(T_{\rm act}, t_{\rm R})$, as described in Figure 2.

ii) The calculated $V_{\rm c,j}$ is a function of $(T_{\rm act}, t_{\rm R})$. At each point in the 2D space of $(T_{\rm act}, t_{\rm R})$, data set (23) yields a set of N calculated values of $V_{{\rm c},j}$. As defined in (28), the normalized sample standard deviation of the set is a function of $(T_{\rm act}, t_{\rm R})$.

$$S_V(T_{\rm act}, t_{\rm R}) \equiv \frac{\text{std}\{V_{{\rm c},j}\} + d}{\text{mean}\{V_{{\rm c},j}\} + d^2}\ , \quad d \equiv \max(0, \delta - \text{mean}\{V_{{\rm c},j}\})$$

iii) As described in (30), we infer $(T_{\rm act}^{\rm (true)}, t_{\rm R}^{\rm (true)})$ by minimizing S_V.

$$(T_{\rm act}^{\rm (est)}, t_{\rm R}^{\rm (est)}) = \underset{(T_{\rm act}, t_{\rm R})}{\text{argmin}}\ S_V(T_{\rm act}, t_{\rm R})$$

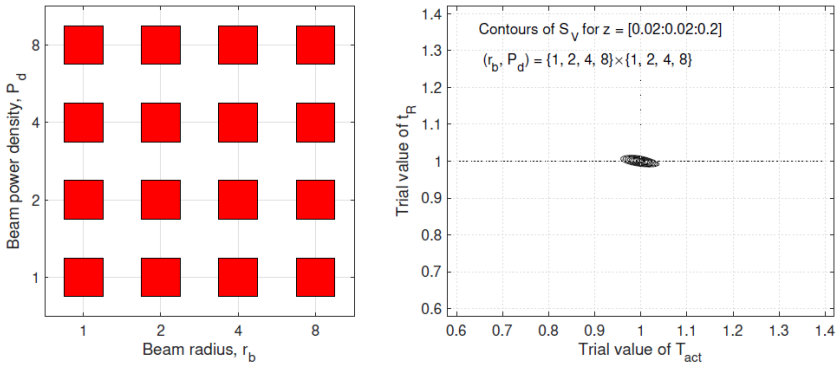

Figure 8: Left: $(r_{\rm b}, P_d)$-distribution of the data set from all 16 pairs of beam parameters in the 2D region. Right: contours of S_V vs $(T_{\rm act}, t_{\rm R})$ based on the data set.

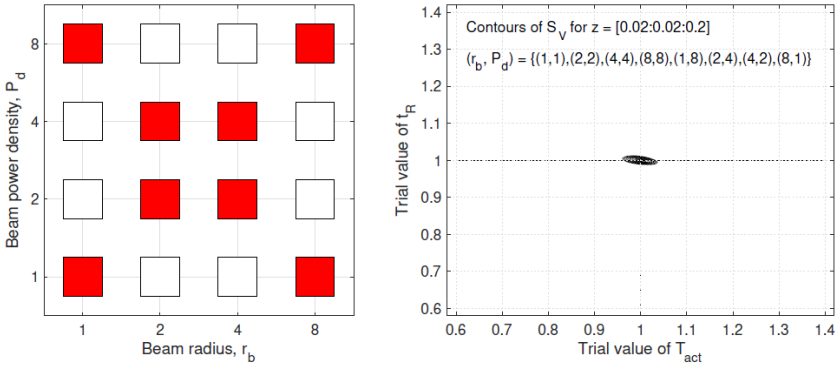

Figure 9: Left: $(r_{\rm b}, P_d)$-distribution of the data set from 8 pairs of beam parameters covering the two diagonal directions of the 2D region. Right: contours of S_V vs $(T_{\rm act}, t_{\rm R})$ based on the data set.

iv) As given in (31), $v_{\rm c}^{(\rm m)} \equiv \text{median}(v_{\rm c})$ is estimated from $\{V_{{\rm c},j}(T_{\rm act}^{(\rm est)}, t_{\rm R}^{(\rm est)})\}$.

$$v_{\rm c}^{(\rm m,est)} = \text{median}\{V_{{\rm c},j}(T_{\rm act}^{(\rm est)}, t_{\rm R}^{(\rm est)})\}$$

v) In the presence of noise, the success of inference requires that S_V have a robustly defined minimum in the 2D space of $(T_{\rm act}, t_{\rm R})$, which depends on the diversity in beam parameters $(r_{\rm b}, P_d)$ used in exposure tests. The most effective data set has the $(r_{\rm b}, P_d)$-distribution shown in Figure 9. We shall use this $(r_{\rm b}, P_d)$-distribution when generating artificial data sets in our numerical tests.

Inference results on data from the Weibull distribution

In this subsection, we test the performance of the inference method on data generated with random subjective threshold $v_{\rm c}$ of the Weibull distribution. Histograms of $v_{\rm c}$ are displayed in Figure 10 for std/med = 0.1, 0.2, 0.4 and 0.8 where "med" denotes "median"(Figure 10).

$$\frac{\text{std}}{\text{med}} \equiv \frac{\text{std}(v_{\rm c})}{\text{median}(v_{\rm c})}$$

Note that with std/med = 0.4, the relative uncertainty is already unusually large for the subjective threshold. With std/med = 0.8, the relative uncertainty in $v_{\rm c}$ is unrealistic. We include these large values of std/med in our numerical tests to demonstrate the trends of inference errors vs underlying uncertainty in $v_{\rm c}$.

In data generation, we use the $(r_{\rm b}, P_d)$-distribution in Figure 9, which consists of 8 pairs of $(r_{\rm b}, P_d)$. At each pair of $(r_{\rm b}, P_d)$, we run m independent exposure tests to sample the randomness of $v_{\rm c}$. The resulting data set contains $N = 8m$ exposure tests. In numerical simulations below, $N = 200$ $(m = 25)$ unless indicated otherwise.

In Figure 11, we plot contours of S_V vs $(T_{\rm act}, t_{\rm R})$ for std/med = 0.1, 0.2, 0.4 and 0.8. In each panel, the minimum of S_V in the 2D space of $(T_{\rm act}, t_{\rm R})$, shown as a red dot, gives the inference results $(T_{\rm act}^{(\rm est)}, t_{\rm R}^{(\rm est)})$. It is clear that a larger uncertainty in $v_{\rm c}$ makes the surface of S_V flatter, which in turn makes the minimum more susceptible to perturbations.

Following the intuition gained in Figure 11, we use Monte Carlo simulations to investigate the effects of std/med of $v_{\rm c}$ on the inference results.At every set of parameters, we repeat the process of data generation and inference for $M = 500$ Monte Carlo runs, each yielding one set of estimated parameters $(T_{\rm act}^{(\rm est)}, t_{\rm R}^{(\rm est)}, v_{\rm c}^{(\rm m,est)})$. From $M = 500$ Monte Carlo runs, values of $(T_{\rm act}^{(\rm est)}, t_{\rm R}^{(\rm est)}, v_{\rm c}^{(\rm m,est)})$ vs std/med of $v_{\rm c}$ are presented as scatter plots with associated box plots in 3 panels of Figure 12. These 3 quantities are inferred from data set (23), which does not contain values of since it is not measurable in real experiments. Of these 3 quantities, $t_{\rm R}^{(\rm est)}$ has the smallest relative error; $v_{\rm c}^{(\rm m,est)}$ has the largest relative error. For comparison, we also plot sample median of $v_{\rm c}$ vs std/med of $v_{\rm c}$ in the bottom right panel of Figure 12. The sample median is calculated in

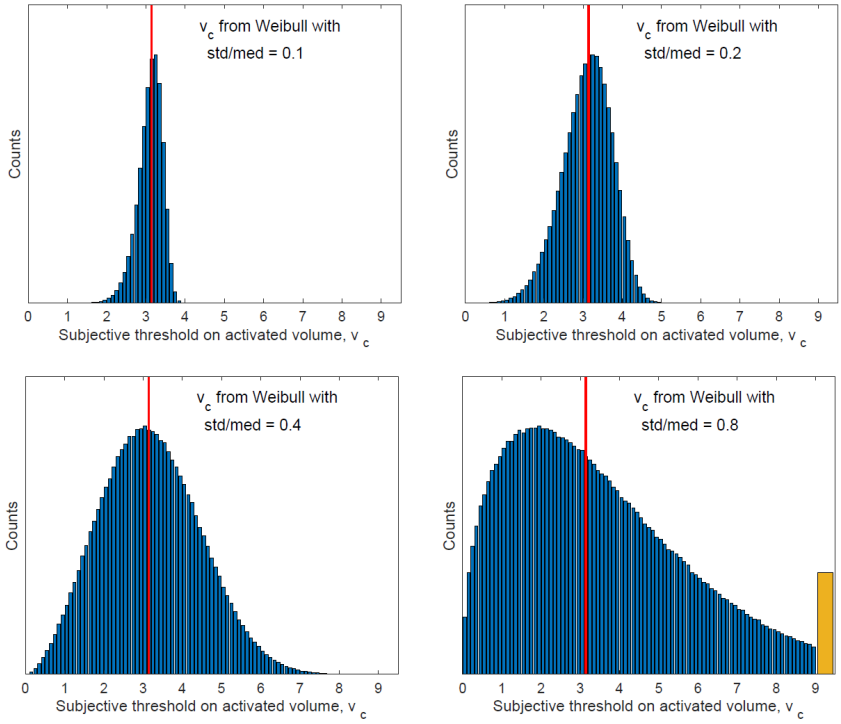

Figure 10: Histograms of $v_{\rm c}$ for std/med = 0.1, 0.2, 0.4 and 0.8. The orange bar represents the bin of $[9, +\infty)$.

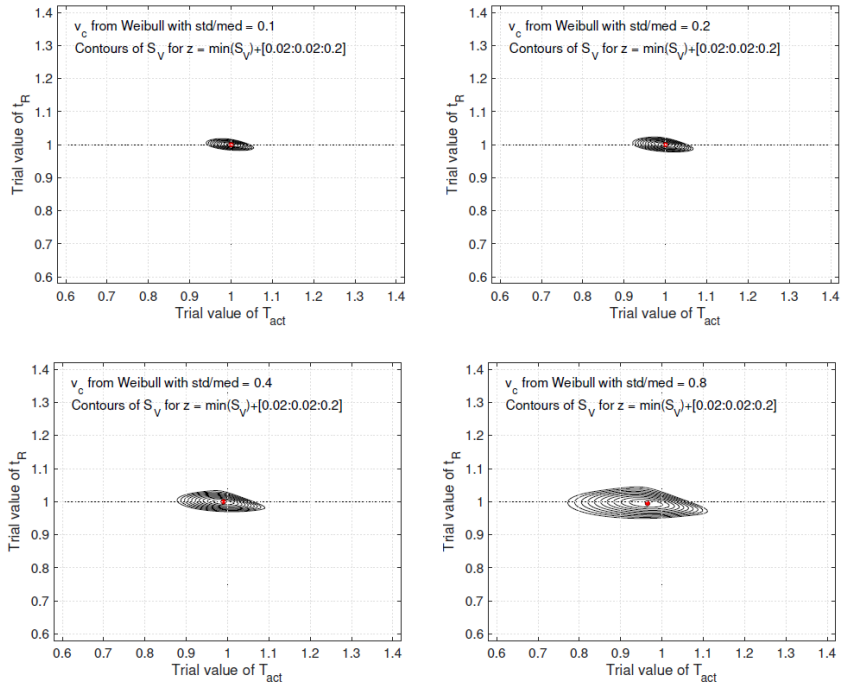

Figure 11: Contours of S_V vs $(T_{\rm act}, t_{\rm R})$ based on data with the std/med given.

the data generation process (23).

$$v_{\rm c}^{\rm (m,samp)} \equiv \text{median}\big\{v_{{\rm c},j},\ j = 1, 2, \ldots, N\big\}$$

Note that sample values of $v_{\rm c}$ are not measurable in experiments. As a result, the sample median cannot be calculated from data set (23), which makes the sample median irrelevant in real applications. Here we plot the sample median to demonstrate an upper limit on the inference performance of $v_{\rm c}^{\rm (m,est)}$ Even if we are given sample values of $v_{\rm c}$ in the data set, statistically we cannot estimate $v_{\rm c}^{\rm m}$ more accurately than the sample median.

In each of the 3 panels for $(T_{\rm act}^{\rm (est)}, t_{\rm R}^{\rm (est)}, v_{\rm c}^{\rm (m,est)})$ in Figure 12, values of the estimated quantity show both a spreading (the IQR box in box plots) and a systematic bias (the median line in box plots). We examined the effects of sample size N

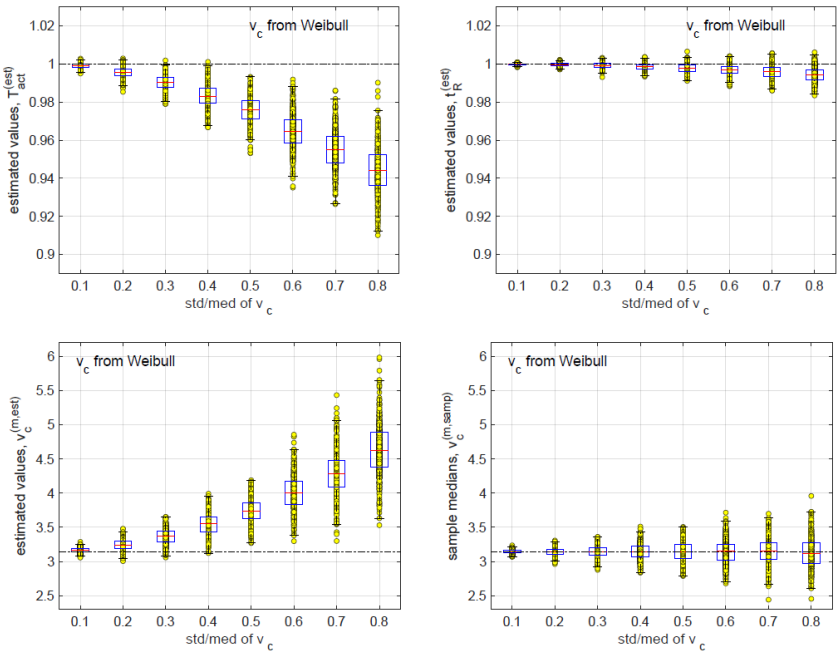

Figure 12: Top left: values of $T_{\rm act}^{(\rm est)}$ inferred from data vs std/med of $v_{\rm c}$. Top right: $t_{\rm R}^{(\rm est)}$ vs std/med. Bottom left: $v_{\rm c}^{(\rm m,est)}$ vs std/med. Bottom right: sample median of $v_{\rm c}$ vs std/med.

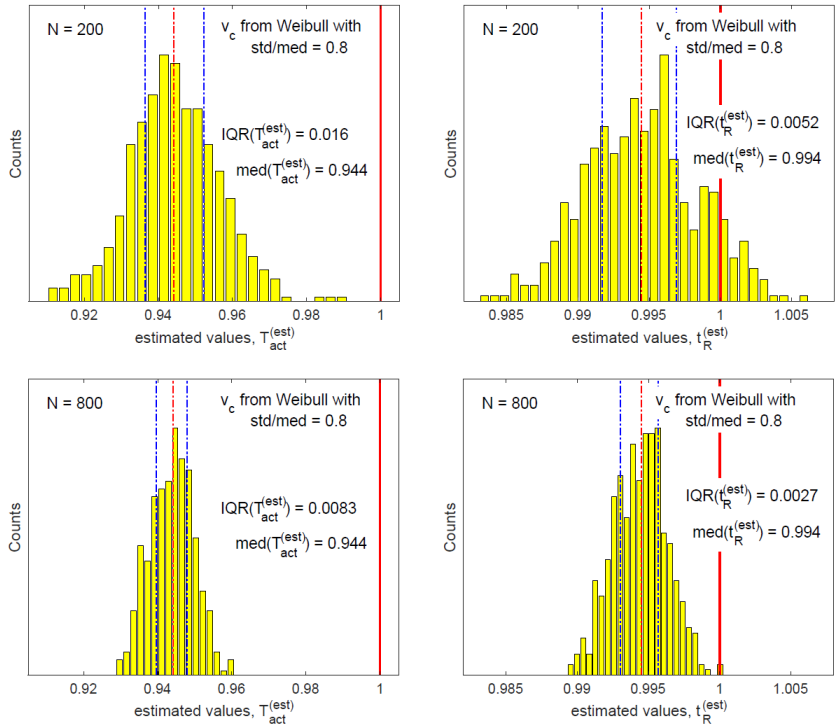

Figure 13: Histograms of $T_{\rm act}^{(\rm est)}$ (left) and $t_{\rm R}^{(\rm est)}$ (right) from Monte Carlo simulations with sample size $N = 200$ (top) and $N = 800$ (bottom).

on the spreading and the bias. Figure 13 compares values of $(T_{\rm act}^{(\rm est)}, t_{\rm R}^{(\rm est)})$ for $N = 200$ (top row) and for $N = 800$ (bottom row); Figure 14 compares values of $(v_{\rm c}^{(\rm m,est)}, v_{\rm c}^{(\rm m,samp)})$ for $N = 200$ (top row) and for $N = 800$ (bottom row), where N is the number of exposure tests in a data set. In each panel, the two dotted blue lines indicate respectively the 25th and the 75th percentiles corresponding to the IQR box in box plots of Figure 12; the dotted red line indicates the median. Figures 13 and 14 demonstrate that as sample size N increases, the interquartile range (IQR) of the inferred quantity decreases, proportional to $N^{-1/2}$. In contrast, the bias in the inferred quantity remains unchanged as sample size N is increased.

Next we study the effects of std/med (relative uncertainty in subjective threshold $v_{\rm c}$) on the relative spreading and the

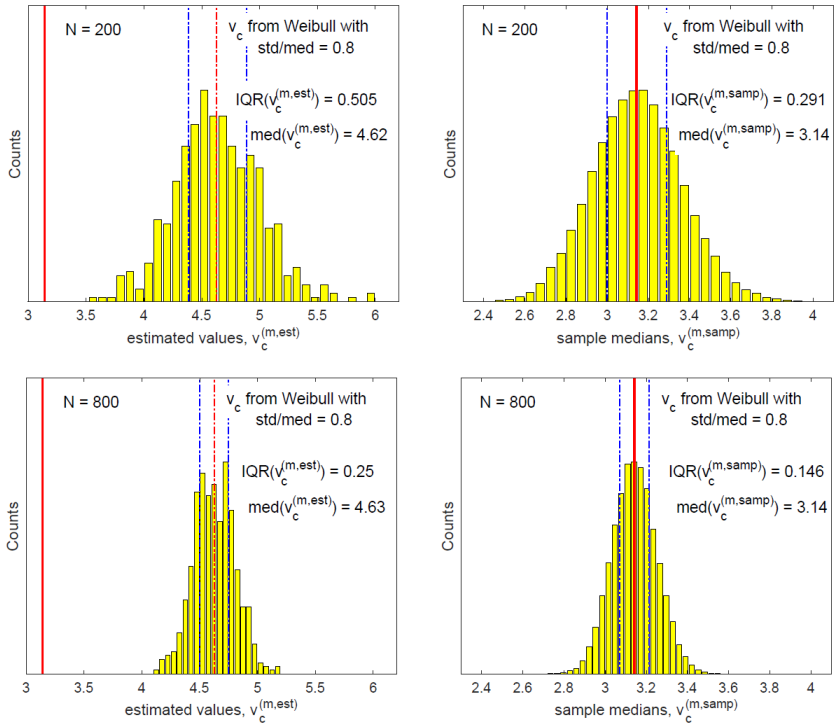

Figure 14: Left: histograms of $v_c^{(m,est)}$ from Monte Carlo simulations with sample size $N = 200$ (top) and $N = 800$ (bottom). Right: histograms of $v_c^{(m,samp)}$ are plotted for reference only. $v_c^{(m,samp)}$ is not available from experimental data.

relative bias of an inferred quantity. We introduce two measures of relative error in a quantity Q, which can be any of $(T_{act}^{(est)}, t_R^{(est)}, v_c^{(m,est)})$.

$$\text{err}_1(Q) \equiv \frac{|\text{mean}(Q) - Q^{(true)}|}{Q^{(true)}} \tag{32}$$

$$\text{err}_2(Q) \equiv \frac{\text{std}(Q)}{Q^{(true)}} \tag{33}$$

$\text{err}_1(Q)$ measures the relative bias in quantity Q while $\text{err}_2(Q)$ measures the relative spreading in quantity Q. In Figure 15, for the 3 inferred quantities $(T_{act}^{(est)}, t_R^{(est)}, v_c^{(m,est)})$, we plot err_1 (left column) and err_2 (right column) vs std/med of v_c as linear plots (top row) and as log-log plots (bottom row). The straight line fittings in log-log plots demonstrate that for each of the 3 inferred quantities, err_1 is proportional to $(\text{std/med})^2$ while err_2 is proportional to std/med. In other words, the relative bias is proportional to $(\text{std/med})^2$.

When the relative uncertainty in v_c is small, the relative biases in the 3 inferred quantities are small. At std/med = 0.1, all 3 relative biases are below 0.01. At std/med = 0.8 (which is an unrealistically large uncertainty in v_c as shown in Figure 10), the relative bias in $v_c^{(m,est)}$ is close to 0.5.

Inference Results on Data from the Log-Normal Distribution

In this subsection, we test the performance of the inference method on data generated with random subjective threshold v_c of the log-normal distribution. Histograms of v_c are displayed in Figure 16 for std/med = 0.1, 0.2, 0.4 and 0.8.

Note again that with std/med = 0.4, the relative uncertainty is already unusually large for the subjective threshold. With std/med = 0.8, the relative uncertainty in v_c is unrealistic. We include these large values of std/med in our numerical tests to demonstrate the trends of inference errors vs the underlying uncertainty in v_c.

In data generation, we use the (r_b, P_d)-distribution in Figure 9, which consists of 8 pairs of (r_b, P_d). At each pair of (r_b, P_d), we run m independent exposure tests to sample the randomness of v_c. The resulting data set contains $N = 8m$ exposure tests. In numerical simulations below, $N = 200$ $(m = 25)$ unless indicated otherwise.

We use Monte Carlo simulations to investigate the effects of std/med of v_c on the inference results. At every set of parameters, we repeat the process of data generation and inference for $M = 500$ Monte Carlo runs, each yielding one set of estimated parameters $(T_{act}^{(est)}, t_R^{(est)}, v_c^{(m,est)})$. From $M = 500$ Monte Carlo runs, values of $(T_{act}^{(est)}, t_R^{(est)}, v_c^{(m,est)})$ vs std/med of v_c are presented as scatter plots with associated box plots in 3 panels of Figure 17. Of the 3 quantities inferred from data set (23), $t_R^{(est)}$ has the smallest relative error; $v_c^{(m,est)}$ has the largest relative error.

For comparison we also plot sample median of v_c vs std/med of v_c in the bottom right panel of Figure 17. The sample median is calculated in the data generation process; it is not calculated from data set (23), which does not contain samples of v_c since v_c is not measurable in experiments.

In each of the 3 panels for $(T_{act}^{(est)}, t_R^{(est)}, v_c^{(m,est)})$ in Figure 17, values of the estimated quantity show both a spreading (the IQR box in box plots) and a systematic bias (the median line in box plots). We examine the effects of sample size N on the

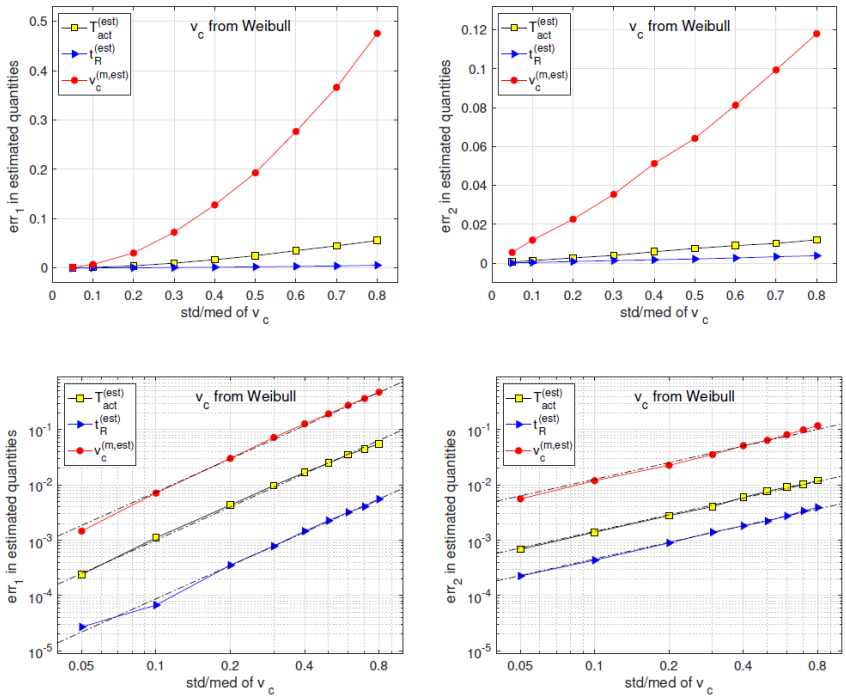

Figure 15: Errors in the 3 inferred quantities. err_1 (left) and err_2 (right) vs std/med of v_c. Top: linear plots. Bottom: log-log plots. err_1 and err_2 are defined in (32)-(33).

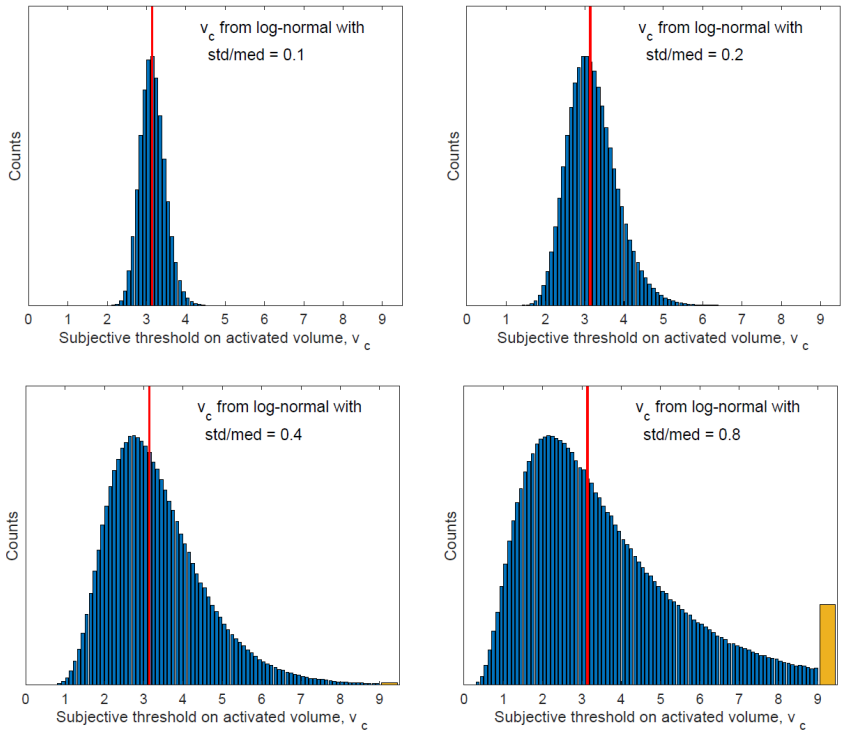

Figure 16: Histograms of v_c for std/med = 0.1, 0.2, 0.4 and 0.8. The orange bar represents the bin of $[9, \infty)$.

spreading and on the bias.

Figure 18 compares values of $(T_{\text{act}}^{(\text{est})}, v_c^{(\text{m, est})})$ for $N = 200$ (top row) and for $N = 800$ (bottom row). We focus on $T_{\text{act}}^{(\text{est})}$ and $v_c^{(\text{m, est})}$ because they have the largest inference errors. In each panel, the two dotted blue lines indicate respectively the 25th and the 75th percentiles corresponding to the IQR box in box plots of Figure 17; the dotted red line indicates the median. Figures 18 demonstrates that data from the log-normal distribution have the same behavior as those from the Weibull distribution in Figures 13 and 14. As sample size N increases, the interquartile range (IQR) of the inferred quantity decreases, proportional to $N^{-1/2}$. In contrast, the bias in the inferred quantity remains unchanged as sample size N is increased.

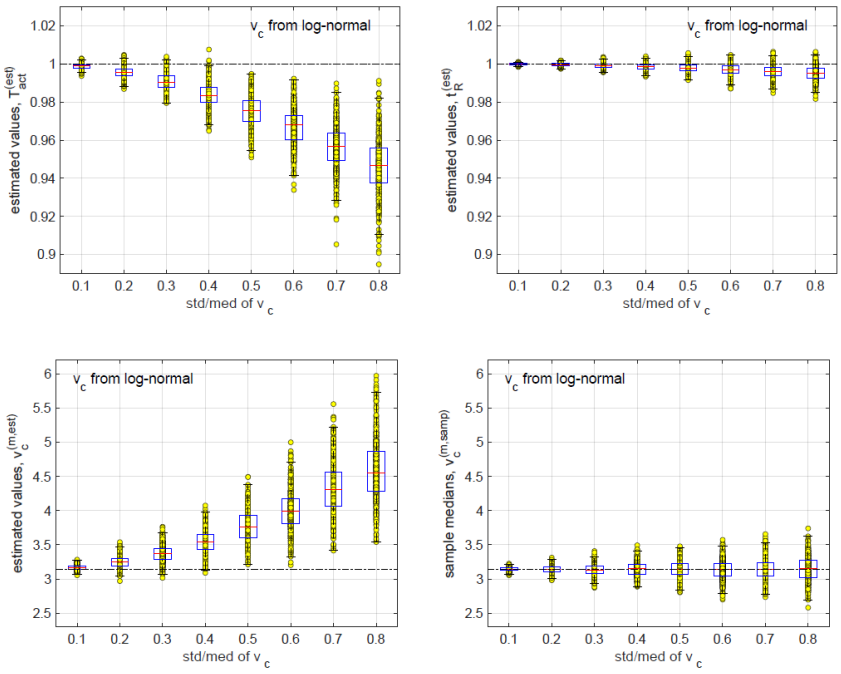

Figure 17: Top left: values of $T_{\rm act}^{(\rm est)}$ inferred from data vs std/med of $v_{\rm c}$. Top right: $t_{\rm R}^{(\rm est)}$ vs std/med. Bottom left: $v_{\rm c}^{(\rm m,est)}$ vs std/med. Bottom right: sample median of $v_{\rm c}$ vs std/med.

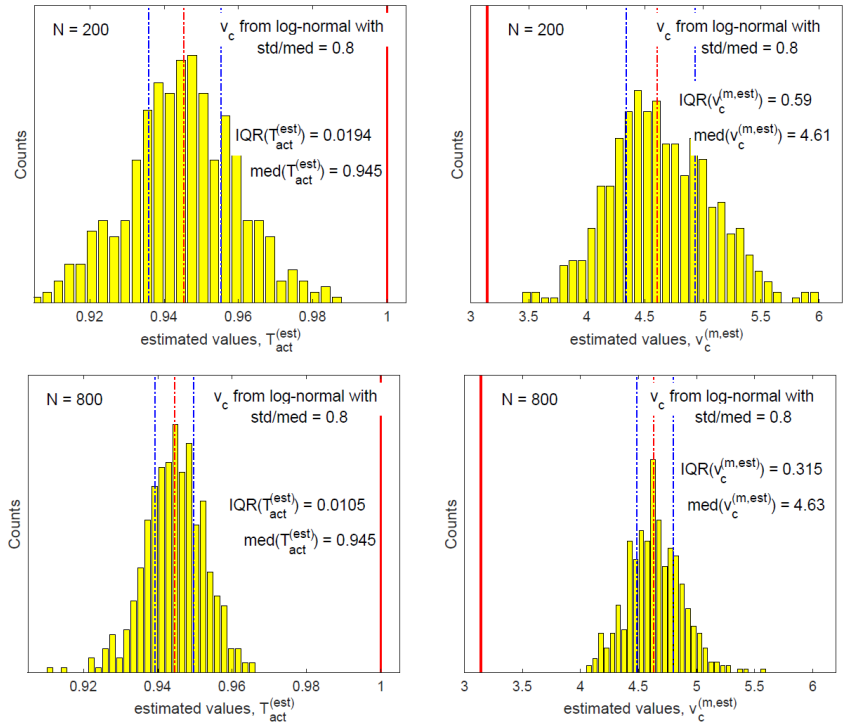

Figure 18: Histograms of $T_{\rm act}^{(\rm est)}$ (left) and $v_{\rm c}^{(\rm m,est)}$ (right) from Monte Carlo simulations with sample size $N = 200$ (top) and $N = 800$ (bottom).

We studied the effects of randomness in data on the relative spreading and the relative bias in the inference. We use $\mathrm{err}_1(Q)$ and $\mathrm{err}_2(Q)$ defined in (32)-(33) to measure the relative bias and the relative spreading of an inferred quantity Q. We study the effects of std/med (relative uncertainty in subjective threshold $v_{\rm c}$) on $\mathrm{err}_1(Q)$ and $\mathrm{err}_2(Q)$. In 19, for the 3 inferred quantities $(T_{\rm act}^{(\rm est)}, t_{\rm R}^{(\rm est)}, v_{\rm c}^{(\rm m,est)})$, we plot err_1 (left column) and err_2 (right column) vs std/med as linear plots (top row) and as log-log plots (bottom row). The straight line fittings in log-log plots demonstrate that for each of the 3 inferred quantities, err_1 is proportional to $(\mathrm{std/med})^2$ while err_2 is proportional to std/med. In other words, the relative bias is proportional to $(\mathrm{std/med})^2$. When the relative uncertainty in $v_{\rm c}$ is small, the relative biases in the 3 inferred quantities are small. At std/med

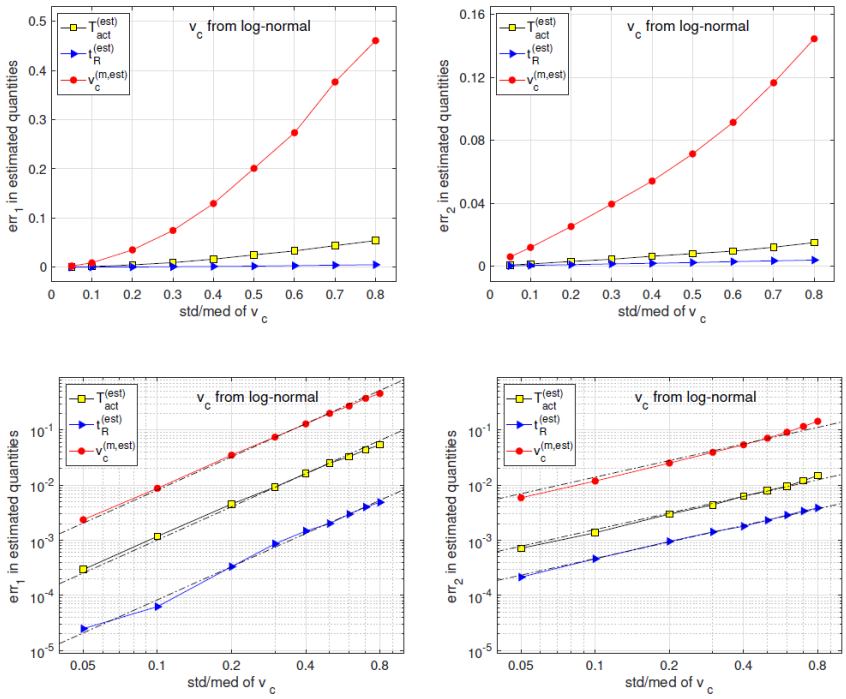

Figure 19: Errors in the 3 inferred quantities. err_1 (left) and err_2 (right) vs std/med. Top: linear plots. Bottom: log-log plots. err_1 and err_2 are defined in (32)-(33).

= 0.1, all 3 relative biases are below 0.01. At std/med = 0.8 (which is an unrealistically large uncertainty in v_c as shown in Figure 16, the relative bias in $v_c^{(m,est)}$ is close to 0.5.

Conclusions and Discussion

We study the heat-induced flight action when a subject is exposed to a millimeter wave beam. We explore extracting 3 key model parameters simultaneously from experimental data measured in exposure tests using the method of limits. The 3 key model parameters are i) the activation temperature of thermal nociceptors, ii) the threshold on activated skin volume for initiating flight, and iii) the human reaction time (the time from the flight initiation to the flight actuation). The experimental data from each exposure test include a) beam specifications (beam power density and beam radius), b) the time of observed flight action, and c) the skin internal temperature as a function of time and 3D spatial coordinates (reconstructed from a time series of skin surface temperature distributions recorded by an IR camera).

We use a model based on thermal nociceptors activation to describe the heat-induced flight in both the data generation and the inference formulation. The millimeter wave electromagnetic energy absorbed by the skin goes to increase the skin temperature. When the local skin temperature reaches the activation temperature, the thermal nociceptors in that region are activated to transduce an electrical signal. The aggregated signal is proportional to the number of nociceptors activated and (when nociceptors are uniformly distributed) is proportional to the volume of activated skin. We use the activated volume to measure the internal stimulus to brain. The response of flight or no flight is determined by a subjective threshold on the activated volume. Due to the lateral and longitudinal biovariability, the subjective threshold is a random variable fluctuating from one subject to another and from a test to another on the same subject. In each individual exposure test, even if the exposure conditions are kept unchanged, the outcome is still uncertain due to the randomness in the subjective threshold. When the activated volume exceeds the subjective threshold, flight is initiated in the sense that the aggregated electrical signal transduced at the exposed skin spot, upon propagating to the brain, is strong enough to trigger the brain to issue a flight instruction. This process takes time. It takes additional time for the flight instruction to reach the muscles and for the muscles to materialize the flight action. The time gap between the internal flight initiation (not observable in experiments) and the observed flight action is the human reaction time. The 3 key parameters of the model are i) the nociceptor activation temperature T_{act}, ii) the subjective volume threshold for initiating flight v_c, and iii) the human reaction time t_R. In this study, we allow the subjective threshold to be a random variable while treating the other two as deterministic unknowns. For the fluctuating subjective threshold, we aim at estimating its median $v_c^{(m)}$. The goal of inference is to estimate 3 deterministic quantities: T_{act}, t_R, and $v_c^{(m)}$.

In an exposure test using the method of limits, the beam power is kept on until the flight action is observed. The time of observed flight action is recorded. Neither the time of internal flight initiation nor the human reaction time is directly measurable in experiments. Furthermore, the effects of activation temperature and the median subjective threshold are tangled in the non-observable time of internal flight initiation: given the beam power density (P_d) and beam radius (r_b), simultaneously lowering the activation temperature and increasing the subjective threshold in a certain combination will yield the same value for the flight initiation time (at which the activated volume reaches the subjective threshold). Mathematically, $(T_{\text{act}}, t_R, v_c^{(m)})$ can-

not be determined simultaneously from data measured in a sequence of exposure tests all having the same pair of (r_b, P_d). To infer all 3 parameters, it is necessary to have a sequence of diversified exposure tests with various points in the (r_b, P_d) plane.

To develop the inference method, we examine the activated volume at flight initiation, which is calculated from the skin internal temperature distribution using trial values of (T_{act}, t_R). The skin internal temperature distribution is constructed from the time series of measured skin surface temperatures in experiments. The trial value of human reaction time t_R predicts the time of flight initiation from the time of observed flight action in the data. The trial value of activation temperature T_{act} predicts the activated volume at the flight initiation. For exposure test j, the predicted activated volume at flight initiation $V_{c,j}(T_{act}, t_R)$ is a function of trial values of (T_{act}, t_R). This function varies from one test to another as the values of (r_b, P_d) change. A sequence of exposure tests yield a family of functions $\{V_{c,j}(T_{act}, t_R)\}$. The inference formulation is motivated by the observation that in the absence of fluctuations in subjective threshold v_c, at the true values of (T_{act}, t_R), we have $V_{c,j}(T_{act}^{(true)}, t_R^{(true)}) = v_c^{(m)}$ for all j's (all tests in the data set). In other words, the sample standard deviation of $\{V_{c,j}(T_{act}, t_R)\}$ over j attains a minimum at $(T_{act}^{(true)}, t_R^{(true)})$. To measure the relative standard deviation and to stay away from the region where $V_{c,j}(T_{act}, t_R) = 0$ for all j's, we define function $S_V(T_{act}, t_R)$ in (28). $S_V(T_{act}, t_R)$ attains a minimum at $(T_{act}^{(true)}, t_R^{(true)})$ and has a large value where $V_{c,j}(T_{act}, t_R) = 0$ for all j's. The inference of (T_{act}, t_R) is carried out by minimizing $S_V(T_{act}, t_R)$. Once the estimated values $(T_{act}^{(est)}, t_R^{(est)})$ are obtained, the median subjective threshold is estimated as $v_c^{(est)} = \text{med}\{V_{c,j}(T_{act}^{(est)}, t_R^{(est)})\}$.

We extend the scope of inference study to include both extracting information from given data and designing experiments to reveal more information. In this study, the experimental design involves finding the distribution of (r_b, P_d) for exposure tests to make the minimum of $S_V(T_{act}, t_R)$ at $(T_{act}^{(true)}, t_R^{(true)})$ uniquely and robustly defined such that $(T_{act}^{(true)}, t_R^{(true)})$ is reliably estimated even in the presence of noise and perturbation. We generate artificial data sets with various patterns for the distribution of (r_b, P_d). When the sequence of exposure tests spans only the P_d-direction with a fixed value of r_b, the inference based on the measured data yields a reasonable estimate for the human reaction time t_R while the estimation of activation temperature T_{act} is unreliable. When the sequence of exposure tests spans only the r_b-direction with a fixed value of P_d, the inference based on the measured data can estimate one of (T_{act}, t_R) only when the other is known. When the sequence of exposure tests spans a rectangular region of (r_b, P_d) along its horizontal and vertical directions, the inference based on the measured data is capable of accurately estimate both T_{act} and t_R simultaneously. When the sequence exposure tests spans the same rectangular region of (r_b, P_d) along its two diagonal directions as shown in Figure 9, the inference based on the measured data yields a significantly more robust result. We suggest that future experiments should consider adopting the (r_b, P_d)-distribution shown in Figure 9 when designing the beam specifications of exposure tests. We test the inference performance on artificial data generated with fluctuating subjective threshold v_c. The relative uncertainty of v_c is measured by std/med $\equiv$ std(v_c)/median(v_c).

To test the effect of relative uncertainty of v_c, we generate data from respectively the Weibull distribution and the log-normal distribution, each with std/med $= 0, 0.1, 0.2, 0.4, 0.8$. As demonstrated in Figure 12, the error in the inferred result has two parts: the systematic bias (err_1) and the spreading (err_2), defined in (32)-(33). In our numerical tests, err_1 and err_2 are calculated over $M = 500$ Monte Carlo runs of data generation and inference. Both errors are attributed to the uncertainty of v_c. In the case of std/med $= 0$, both errors are zero. In the case of std/med > 0, of the 3 key model parameters $(T_{act}, t_R, v_c^{(m)})$, the inferred human reaction time $t_R^{(est)}$ has the lowest relative error while the inferred median subjective threshold $v_c^{(m,est)}$ has the largest relative error, as shown in Figure 12.

We examine the effect of sample size N (the number of exposure tests in a date set). We find that as sample size N increases, the spreading of inferred result (err_2) decreases with $1/\sqrt{N}$ while the systematic bias (err_1) does not change, as shown in Figures 13,14.

We examine the effect of relative uncertainty of v_c on err_1 and err_2. The spreading of inferred result (err_2) is proportional to std/med. This is reasonable since both quantities measure fluctuations. In contrast, the systematic bias of inferred result (err_1) is proportional to $(\text{std/med})^2$. This is both good news and bad news. The good news is that when std/med (the relative uncertainty in v_c) is small or moderate, the systematic bias is practically negligible (Figure 15). The bad news is that when std/med is large, the systematic bias is significant and cannot be gotten rid of by increasing the sample size (the number of exposure tests). In a subsequent study, we will explore alternative inference formulations for eliminating or reducing this systematic bias.

Acknowledgement and Disclaimer

The authors acknowledge the Joint Intermediate Force Capabilities Office of U.S. Department of Defense and the Naval Postgraduate School for supporting this work. The views expressed in this document are those of the authors and do not reflect the official policy or position of the Department of Defense or the U.S. Government.

Conflict of Interest

None.

References

[1] Herrick, R. M. (1967) Psychophysical methodology: VI. Random method of limits. *Perceptual & Motor Skills*, **24**, 915-922.

[2] Herrick, R. M. (1973) Psychophysical methodology: Comparison of thresholds of the method of limits and of the method of constant stimuli. *Perception & Psychophysics*, **13**, 548-554.

[3] Kuroda, T. and Hasuo, E. (2014) The very first step to start psychophysical experiments. *Acoust. Sci. & Tech.*, **3**5, 1-9.

[4] (2009) Method of Constant Stimuli. In: Binder M.D., Hirokawa N., Windhorst U. (eds) Encyclopedia of Neuroscience. Springer, Berlin, Heidelber

[5] Wang, H., Adamzadeh, M., Burgei, W., Foley, S. and Zhou, H. (2022) Extracting human reaction time from observations in the method of constant stimuli. *Journal of Applied Mathematics and Physics*, **1**0, 3316-3345.

[6] Wang, H., Burgei, W.A. and Zhou, H. (2023) Inferring internal temperature from measured surface temperatures in electromagnetic heating. *Journal of Directed Energy*, **I**n Press.

[7] Parker, J.E., Nelson, E. J. and Beason, C.W. (2017) Thermal and Behavioral Effects of Exposure to 30-kW, 95-GHz Millimeter Wave Energy. Technical Report, AFRL-RH-FS-TR-2017-0016.

[8] Parker, J.E., Nelson, E.J., Beason, C.W. and Cook, M.C. (2017) Effects of Variable Spot Size on Human Exposure to 95-GHz Millimeter Wave Energy. Technical Report, AFRL-RH-FS-TR-2017-0017.

[9] Cazares, S.M., Snyder, J.A., Belanich, J., Biddle, J.C., Buytendyk, A.M., Teng, S.H.M. and O'Connor, K. (2019) Active Denial Technology Computational Human Effects End-To-End Hypermodel for Effectiveness (ADT CHEETEH-E). Human Factors and Mechanical Engineering for Defense and Safety, **3**, Article No 13.

[10] Walters,T.J., Blick, D.W., Johnson,L.R., Adair, E.R. and Foster, K.R. (2000) Heating and Pain Sensation Produced in Human Skin by Millimeter Waves: Comparison to a Simple Thermal Model. *Health Physics*, **7**8(3), 259-267.

[11] Zhadobov, M., Chahat, N., Sauleau, R., Le Quement, C. and Le Drean, Y. (2011) Millimeter-wave Interactions with the Human Body: State of Knowledge and Recent Advances. *International Journal of Microwave and Wireless Technologies*, **3**(2), 237-247.

[12] Topfer, F. and Oberhammer, J. (2015) Millimeter-wave Tissue Diagnosis: The most Promising Fields for Medical Applications. *IEEE Microwave Magazine*, **1**6(4), 97-113.

[13] Wang, H., Burgei, W.A. and Zhou, H. (2020) A concise model and analysis for heat-induced withdrawal reflex caused by millimeter wave radiation. *American Journal of Operations Research*, **1**0, 31-81.

[14] Wang, H., Burgei, W.A. and Zhou, H. (2020) Nondimensional analysis of thermal effect on skin exposure to an electromagnetic beam. *American Journal of Operations Research*, **1**0, 147-162.

[15] Wang, H., Burgei, W.A. and Zhou, H. (2021) Thermal effect of a revolving Gaussian beam on activating heat-sensitive nociceptors in skin. *Journal of Applied Mathematics and Physics*, **9**, 88-100.

[16] Paschotta, R. (2008) Article on "Effective Mode Area" in the Encyclopedia of Laser Physics and Technology, October 2008, Wiley-VCH, ISBN 978-3-527-40828-3.

[17] Durney, C.H., Massoudi, H., and Iskander, M.F. (1986) Radiofrequency Radiation Dosimetry Handbook, 4th ed. Brooks AFB, TX: USAF School of Aerospace Medicine.

[18] Wang, H., Burgei, W.A. and Zhou, H. (2020) Analytical solution of one-dimensional Pennes' bioheat equation. *Open Physics*, **1**8(1), 1084-1092.